



national accelerator laboratory

FERMILAB-Pub-74/106-EXP
2000.000

(Invited paper at the 1974 SLAC Summer
Institute on Particle Physics)

RECENT EXPERIMENTAL RESULTS FROM THE CERN-ISR

G. Giacomelli^{*}

November 1974

^{*}Permanent address: University of Padova, Italy
INFN, Sezione di Padova, Italy



RECENT EXPERIMENTAL RESULTS FROM THE CERN-ISR

G. Giacomelli

University of Padova, Padova, Italy
INFN, Sezione di Padova, Padova
Fermilab, Batavia, Ill.

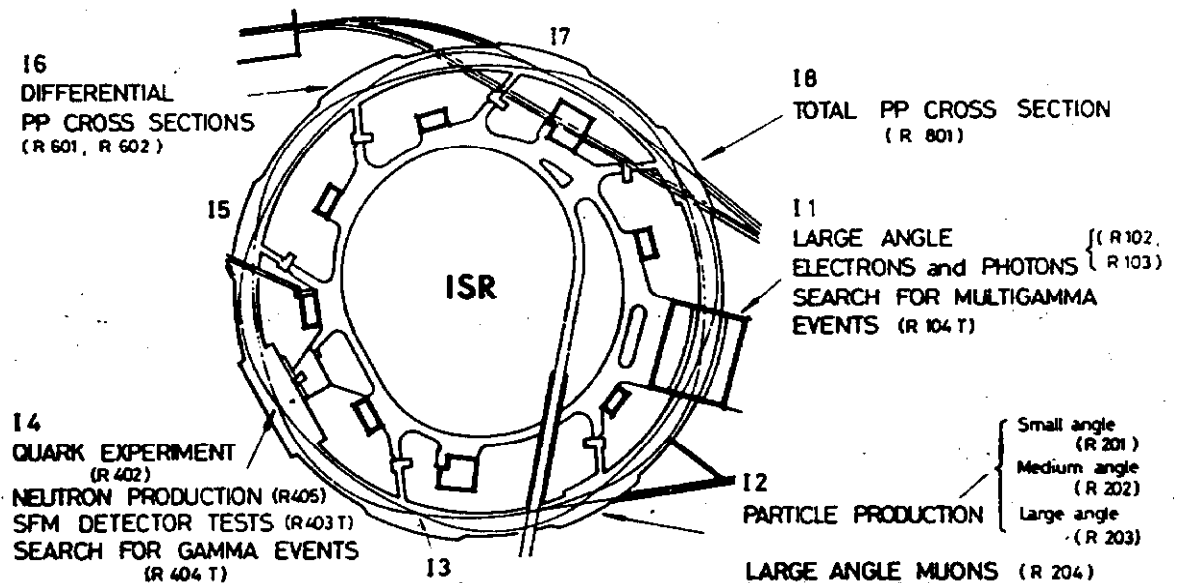
1. INTRODUCTION
2. TOTAL CROSS SECTIONS
3. ELASTIC SCATTERING
4. SINGLE INCLUSIVE REACTIONS
 - 4.1. $f = f(p_t)$
 - 4.1.1. $\langle p_t \rangle_{y_{lab}}$
 - 4.2. $f = f(y_{lab}); f = f(x)$
 - 4.3. $f = f(s)$
 - 4.4. Multiplicities
 - 4.5. Average transverse momenta
5. CORRELATIONS
 - 5.1. Rapidity correlations
 - 5.2. ϕ -correlations
 - 5.3. p_t -correlations
 - 5.4. Rapidity correlations with fast forward negative particles
6. DIFFRACTION PROCESSES. EXCLUSIVE REACTIONS
 - 6.1. Leading particle effects
 - 6.2. Correlations for diffractive events
 - 6.3. Exclusive reactions
 - 6.3.1. $pp \rightarrow (p\pi^+\pi^-)p$
 - 6.3.2. $pp \rightarrow p(n\pi^+)$
7. PROCESSES AT LARGE p_t
 - 7.1. Single inclusive reactions
 - 7.2. Correlations involving large p_t -particles
8. PARTICLE SEARCHES
 - 8.1. Magnetic monopoles
 - 8.2. Quarks
 - 8.3. Direct lepton production
9. CONCLUSIONS

1. INTRODUCTION

I shall try to review the recent experimental results obtained at the CERN-ISR. For the sake of completeness I shall also recall some of the main results obtained earlier.

The ISR started operating for physics three years ago; thus the present experimental layout involves what may be called second generation experiments. It may be of interest to analyze briefly the changes which occurred in the experimental program.

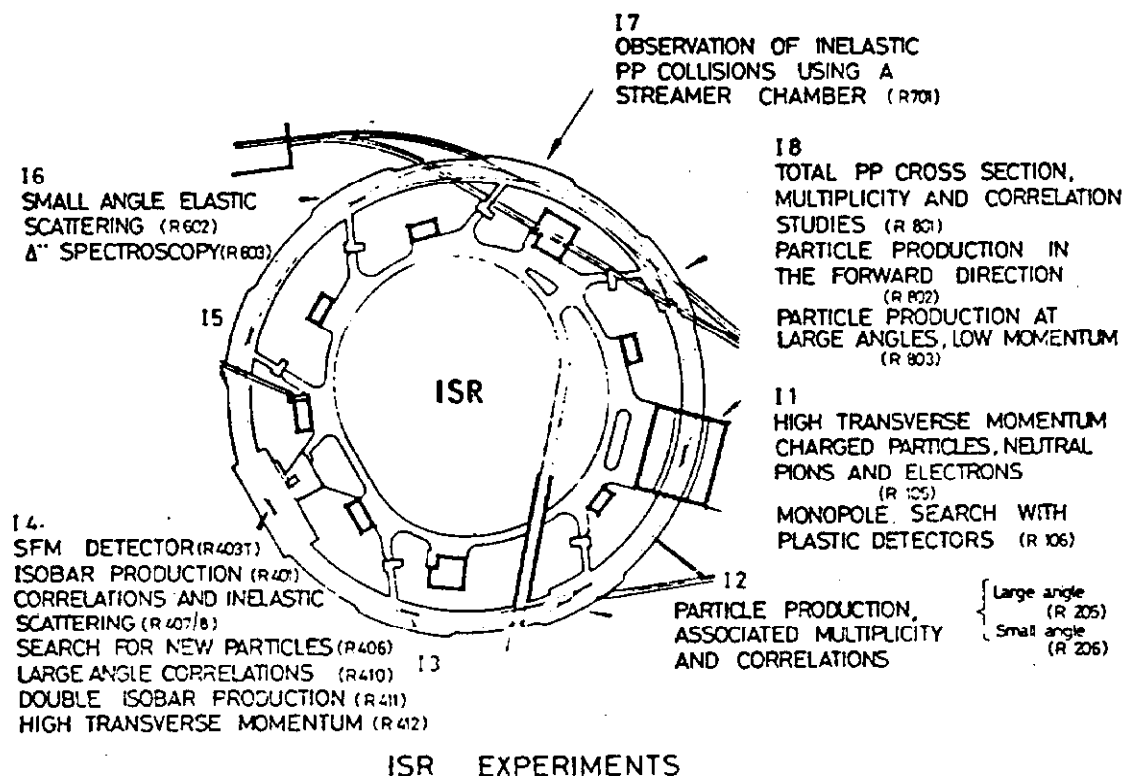
Figure 1.1 illustrates the experiments at the CERN-ISR in 1972. These first generation experiments concerned the measurement of the proton-proton total cross section, of the elastic differential cross section, of the inclusive production of γ , π^+ , k^+ , p^+ and of neutrons, of the search for "exotic" objects, like quarks and intermediate vector mesons. The study of inclusive reactions was the most popular subject of research at that time.



ISR EXPERIMENTS - 1972

Fig. 1.1. Layout of the experiments at the ISR in early 1972.

The layout of 1974, shown in Fig. 1.2, indicates that the presently most popular subject of research concerns the study of correlations in inclusive reactions of various types. In addition there still are experiments of the type studied already in 1972.



FEBRUARY 1974

Fig. 1.2. Layout of the experiments at the ISR in February 1974.

From the technical point of view the experiments have become somewhat more complicated; in some intersecting regions a number of counters or proportional chambers were added to existing single arm spectrometers (see experiments R205 and R206), in others a magnetic spectrometer was added (R801, R105) and in others altogether new detectors are present (R401 ÷ R412, R701). Among the new detectors, one has to mention (i) the coming into operation of the split field magnet facility in intersection region I4 with its 70,000 wires of proportional chambers; (ii) the streamer chambers in I7, which may probably be considered as a kind of "bubble chamber for the ISR."

The number of experiments running at any one time has remained essentially constant, averaging about 10.

The performance of the ISR has been improving steadily. Recently a peak luminosity of $10^{31} \text{ cm}^{-2} \text{ sec}^{-1}$ was achieved, with 22A in each ring. In some runs beam losses were about $3 \times 10^{-6} \text{ min}^{-1}$, which is not too far away from what is to be expected from losses due to pp collisions in the intersecting regions. For a comparison, one may recall that in 1972 average luminosities were 3-6 times smaller. Table 1.1 gives a list of some parameters of the CERN-ISR.

TABLE 1.1

Some Parameters of the CERN-ISR and Present Operation for Physics

Beam momenta	11 - 31 GeV/c, $\Delta p/p \simeq 2\%$
Crossing angle	15°
Beam lifetime $\begin{cases} 5A \\ 10A \end{cases}$	$\sim 1 \text{ month}$ $\sim 2 \text{ days}$
Average pressure	$\lesssim 10^{-10} \text{ torr}$
Pressure in intersections	$\lesssim 10^{-11} \text{ torr}$
Design luminosity	$4 \times 10^{30} \text{ cm}^{-2} \text{ s}^{-1}$
Transverse beam dimensions $\begin{cases} \text{horizontal} \\ \text{vertical} \end{cases}$	$\sim 3\text{-}5 \text{ cm}$ $\sim 0.5 \text{ cm}$

Beam Momenta	c.m. Energy	$s = E_{\text{cm}}^2$	Equivalent Lab. Momentum	Present Average Luminosities
GeV/c	Gev	GeV^2	GeV/c	$10^{30} \text{ cm}^{-2} \text{ s}^{-1}$
11.8/11.8	23.4	548	391	1
15.3/15.3	30.4	921	491	2
22.4/22.4	44.4	1971	1053	4
26.5/26.5	52.6	2767	1474	4
31.4/31.4	62.3	3881	2062	0.5

Table 1.2 gives a list of the experiments at the ISR.

TABLE 1.2. List of ISR Experiments (C = completed, R = running, A = accepted)

Expt. No.	Composition of Group	Description of Experiment	Principal Apparatus	Status
R 101	CERN-Cracow-Bucharest-Tata	Angular distribution 35° - 90°	Nuclear Emulsions	C
R 102	Saclay-Strasbourg	γ and hadrons at large P_t	Wire chambers, magnet	C
R 103	CERN-Columbia Rockefeller	γ at large P_t	Wire chambers, lead glass	C
R 104 T	Brookhaven-Grumman-Rome	High energy multigamma events	As R 103 plus MWPC	C
R 105	CERN-Columbia-Rockefeller-Saclay	γ , e, hadrons at large P_t , correlations	Wire chambers, two magnets, lead glass	R
R 106	Bologna-Rome	Magnetic monopoles	Plastic detectors	R
R 107	Adelphi-Brookhaven-Rome	Search for multigamma events	Lead glass	A
R 201	CERN-Holland-Lancaster-Manchester (CHLM)	Stable particles at small angles	Magnetic spectrometer	C
R 202	Argonne-Bologna-CERN-Michigan-Riverside	Particle prod. at med. angles	Magnetic spectrometer	C
R 203	British Scandinavian Coll.	Stable particles at large angles	Magnetic spectrometer	C
R 204	British Universities Coll.	High P_t Muon Search	Magnetic spectrometer	C
R 205	CERN-Daresbury-Liverpool-RHEL	Correlations with large P_t particle	Magnetic spectrometer	R
R 206	CERN-Holland-Lancaster-Manchester	Correlations with diffractive p	Magnetic spectrometer	R
R 401	CERN-Hamburg-Orsay-Vienna (CHOV)	Isobar production	Split field magnet (SFM)	R
R 402	CERN-Munich	Quark search	Scintillators, MWPC	C
R 403 T	CERN	SFM detector studies	SFM	R
R 404 T	CERN-Hamburg-Vienna	Photon spectra and correlations	Lead glass	C
R 405	CERN-Karlsruhe	Neutrons at small angles	Calorimeter	C

TABLE 1.2. Continued

Expt. No.	Composition of Group	Description of Experiment	Principal Apparatus	Status
R 406	CERN-Bologna	Quark search	SFM	A
R 407	CERN-Coll. de France-Heidelberg-Karlsruhe	Correlations in fragmentation region	SFM	A
R 408	MIT-Orsay-Scandinavians	Correlations at large angles	SFM	A
R 410	Pavia-Princeton	Double isobar production	SFM	R
R 411	Aachen-CERN-Munich	Large p_t correlations	SFM + lead glass	A
R 412	Liverpool-MIT-Orsay-Scandinavian	Large p_t trigger	SFM	A
R 413				
R 601	CERN-Rome	Small angle elastic scattering	Scintillators	C
R 602	Aachen-CERN-Genova-Harvard-Torino (ACGHT)	Elastic scattering	Two arm magnetic spectrometer	C
R 603	Aachen-CERN-UCLA-Harvard	Δ^{++} spectroscopy	Magnetic spectrometer, MWPC	R
R 604	CERN-Genova-Harvard-etc. (CGHMR)	Large angle elastic scattering	Two arm magnetic spectrometer	A
R 701	Aachen-CERN-Munich	Inelastic events	Streamer chambers	R
R 801	Pisa-Stony Brook	σ_{tot} , multiplicities	Scintillator hodoscopes	R
R 802	CERN-Rome	Stable particles, forward direction	Magnetic spectrometer	R
R 803	British-Scandinavian-MIT	Inclusives at low p_t , $x = 0$		A
R 804	Genova-Harvard-MIT-Pisa	Search for muon pairs, Z_0		A
R 805	CERN-Rome	Small angle elastic scattering	Scintillators	A

have to be performed to zero solid angle (Experiment R801, References 73-3, 73-19). The equipment to measure N consisted of an almost 4π detector of scintillation counters and the method is reminiscent of the standard transmission method at conventional accelerators. The luminosity had to be measured separately, with the Van der Meer method of displacing the two beams vertically.

- ii) By measuring the elastic scattering differential cross section in the diffraction region $[0.01 < |t| < 0.12(\text{GeV}/c)^2]$, extrapolating to $t = 0$ and using the optical theorem:

$$\sigma_{\text{tot}}^2 = \frac{16\pi(d\sigma/dt)_{t=0}}{1 + \rho^2} = \frac{16\pi(dN/dt)_{t=0}}{(1 + \rho^2)L} \quad (2.2)$$

where $\rho = [\text{Re } F(s, t = 0)/\text{Im } F(s, t = 0)]$ may be neglected (R601, 73-2).

- iii) By measuring the elastic scattering differential cross section in the Coulomb-Nuclear interference region $[0.001 < |t| < 0.01 (\text{GeV}/c)^2]$, and again using the optical theorem. This method was used at the two lowest ISR energies (R601, 73-1).
- iv) By simultaneously measuring the total collision rate (method i)) and the elastic scattering differential cross section in the diffraction region (method ii)) one has, dividing (2.2) by (2.1):

$$\sigma_{\text{tot}} = \frac{16\pi(dN/dt)_{t=0}}{N(1 + \rho^2)} \quad (2.3)$$

In this case the measurement of σ_{tot} does not depend on the luminosity of the ISR, thus removing one of the largest uncertainties on the cross section measurement.

Results are available from the first three methods. Measurements according to the fourth method are being performed now; their preliminary results confirm the previous measurements.

Figure 2.1 gives a summary of the present knowledge on the energy dependence of the total cross sections of π^+ , k^+ , \bar{p} and p on protons. With the exception of $\bar{p}p$, all total cross sections rise with increasing energy. The k^+p total cross section rises already at Serpukhov energies; the other cross sections start rising at Fermilab energies. The pp cross section rises by about 10% in the ISR energy range. Measurements at the ISR can only provide information on the pp system, but over a large energy span. The data on $\sigma_{\text{tot}}(pp)$ above 10 GeV/c have been fitted with a $\ln^2 s$ dependence yielding

$$\sigma_{\text{tot}}(pp) = 38.4 + 0.49(\ln s/122)^2 \quad (2.4)$$

This fit may be considered a reasonable parametrisation of the data, but not a proof of the \ln^2 dependence.

Where does the increase in σ_{tot} come from? Several hypotheses were put forward by different people:

- i) The increase comes from the increase in the cross sections of the inclusive processes in the central plateau, at $y = 0$.
- ii) The increase comes from the increase in cross section of diffractive processes (their cross section depends on the missing mass (MM) with the form $1/MM^2$; with increasing energy the available mass region increases).
- iii) From the production at large angles of nucleon-antinucleon pairs.
- iv) From the increase in cross section of large p_t -events.

At present it would seem that the increase arises from a mixture of these effects.

3. ELASTIC SCATTERING

Recent results on elastic scattering concern scattering at large angles performed with the split field magnet facility by the CERN-Hamburg-Orsay-Vienna (CHOV) collaboration (R401, 74-13). Two other experiments are planned for the near future:

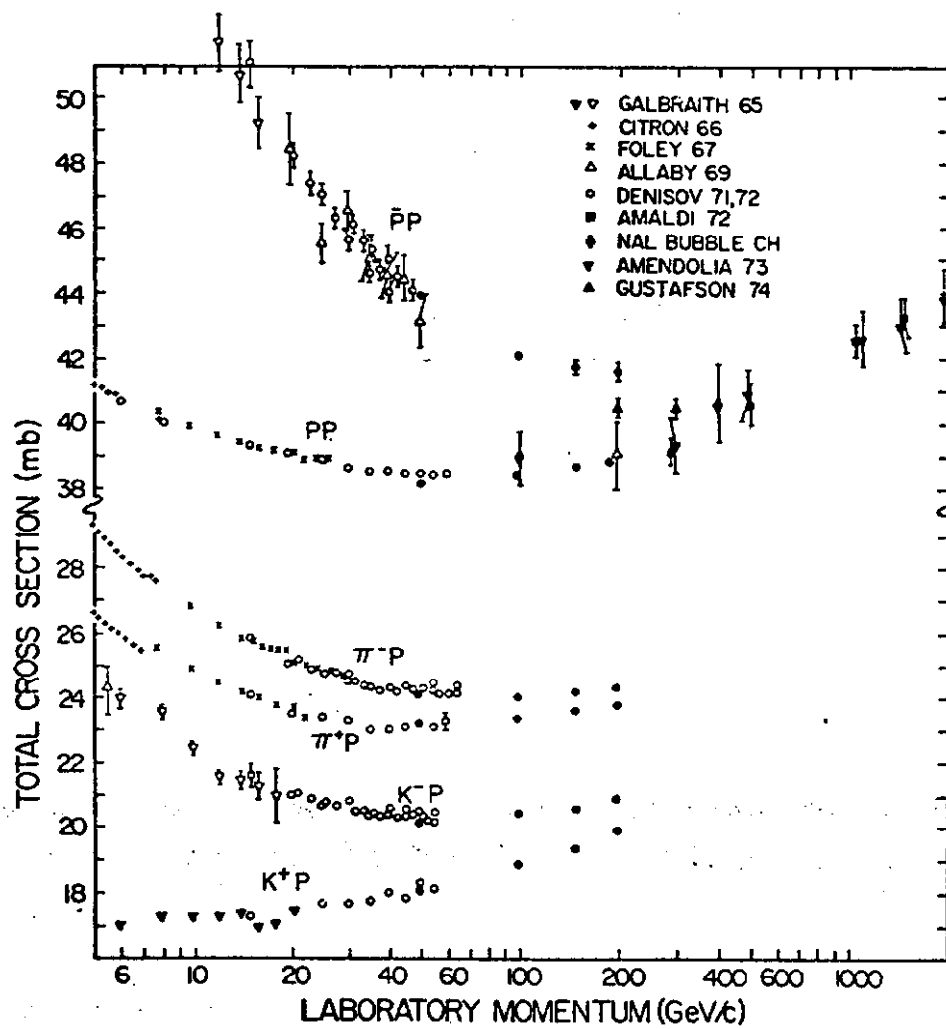


Fig. 2.1. Compilation of total cross section results from experiments at Brookhaven, Serpukhov, Fermilab and CERN-ISR.

- i) One group is going to measure elastic scattering in the diffraction region (R602), and
- ii) another group will measure, in 1975, the elastic scattering in the Coulomb-Nuclear interference region (R805).

Figure 3.1 shows two angular distributions in the Coulomb-Nuclear interference region measured by the CERN-Rome collaboration at equivalent laboratory momenta of 270 and 500 GeV/c (73-1). From these data the authors obtained values of the total cross sections and of the ratio ρ of real to imaginary part of the forward elastic scattering amplitude. The ratios ρ were found to be slightly positive. The analysis of all the high energy data from IHEP, Fermilab and ISR indicates that ρ goes from negative to positive values, crossing zero at about 200 GeV/c.

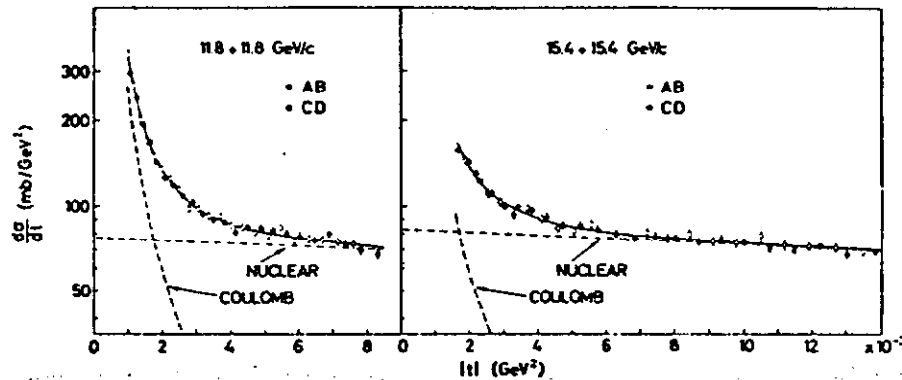


Fig. 3.1. pp elastic scattering in the Coulomb-Nuclear interference region at $\sqrt{s} = 23$ and 31 GeV. The solid line is a fit to the data; the dashed lines indicate the separate contributions of Coulomb and Nuclear scattering respectively (73-1).

Figure 3.2 shows the pp elastic differential cross sections in the diffraction region at equivalent laboratory momenta of 270, 1000 and 1500 GeV/c (72-5). The data show very clearly a change in slope of the diffraction pattern at $|t| \simeq 0.15 \text{ (GeV/c)}^2$. The slope changes approximately by 2 units,

going from about $12.8 (\text{GeV}/c)^{-2}$ for $|t| < 0.15 (\text{GeV}/c)^2$ to $10.8 (\text{GeV}/c)^{-2}$ for $|t| > 0.15 (\text{GeV}/c)^2$. The analysis of the energy dependence of the slope parameter b , computed from measurements in a well defined and fixed t -interval, shows that, for laboratory momenta above 50 GeV/c , b has a logarithmic dependence on s . For $|t| < 0.12 (\text{GeV}/c)^2$ one has:

$$b(s,t) = (8.23 \pm 0.27) + 2 \times (0.278 \pm 0.024) \ln(s/s_0) \quad (3.1)$$

where $s_0 = 1 \text{ GeV}^2$.

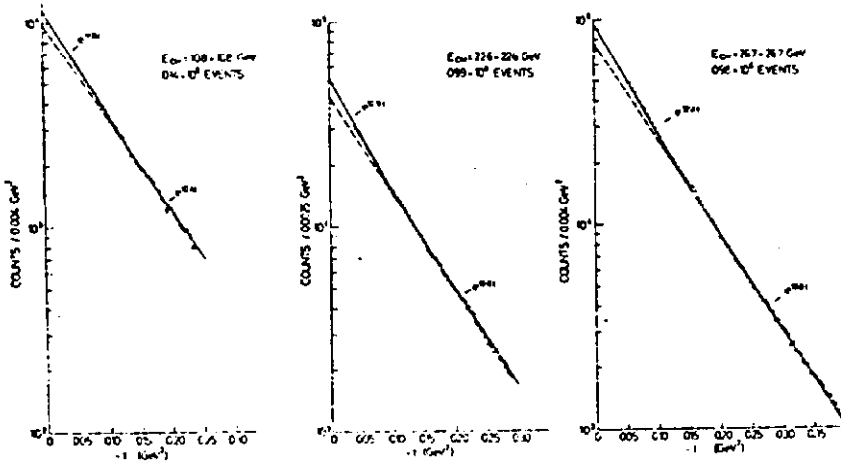


Fig. 3.2. pp elastic angular distributions at $\sqrt{s} = 21.5, 44.9$ and 53 GeV in the diffraction region ($72-5$).

The new elastic scattering data were taken at $\sqrt{s} = 23$ and 62 GeV in the $0.8 < |t| < 3 (\text{GeV}/c)^2$ range. The data were collected together with $pp \rightarrow pn\pi^+$ events using the Split Field Magnet (SFM) facility in the configuration shown in Fig. 3.3. The fast trigger for elastic events was obtained from the multiwire proportional chambers (MWPC) and required at least one particle in both the forward and backward arms of the SFM. This trigger was a very loose one, corresponding to nearly the total pp cross section. A subsequent slow trigger required collinearity of the two tracks and absence of other tracks.

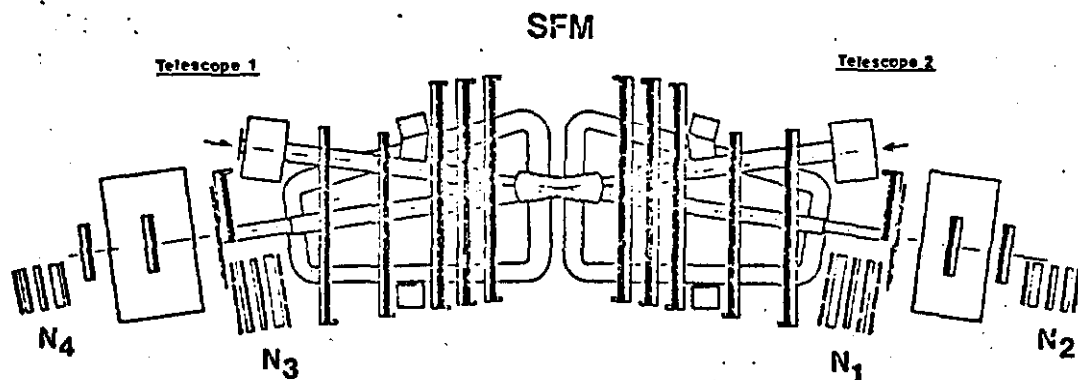


Fig. 3.3. Plan view of the layout of the Split Field Magnet facility as used by the CHOV collaboration (74-13). Thick vertical bars indicate proportional wire chambers. N1-N4 denote neutron counters used to detect the reaction $pp \rightarrow pn\pi^+$.

Off line analysis was later performed using three steps: track recognition, track fitting in the magnetic field and kinematical fitting. Figure 3.4 shows the elastic angular distributions at $\sqrt{s} = 23$ and 62 GeV. These results are preliminary. The data confirm the existence of a dip-bump structure as previously observed by the ACGHT collaboration (74-3).

The whole pp angular distribution is reminiscent of a diffraction pattern. The CHOV group fitted the t -distributions with the formula

$$\frac{d\sigma}{dt} \simeq A \left| e^{Bt/2} + \sqrt{\frac{C}{A}} \exp\left(\frac{Dt}{2} + i\phi\right) \right|^2 \quad (3.2)$$

The results of the fits are shown as solid curves in Fig. 3.4. From the fits one can derive: (i) the location of the dip and (ii) the height of the secondary peak. The results are shown in Fig. 3.5. The location of the minimum is decreasing with increasing energy: it is at $1.45 (\text{GeV}/c)^2$ at $\sqrt{s} = 23$ GeV and

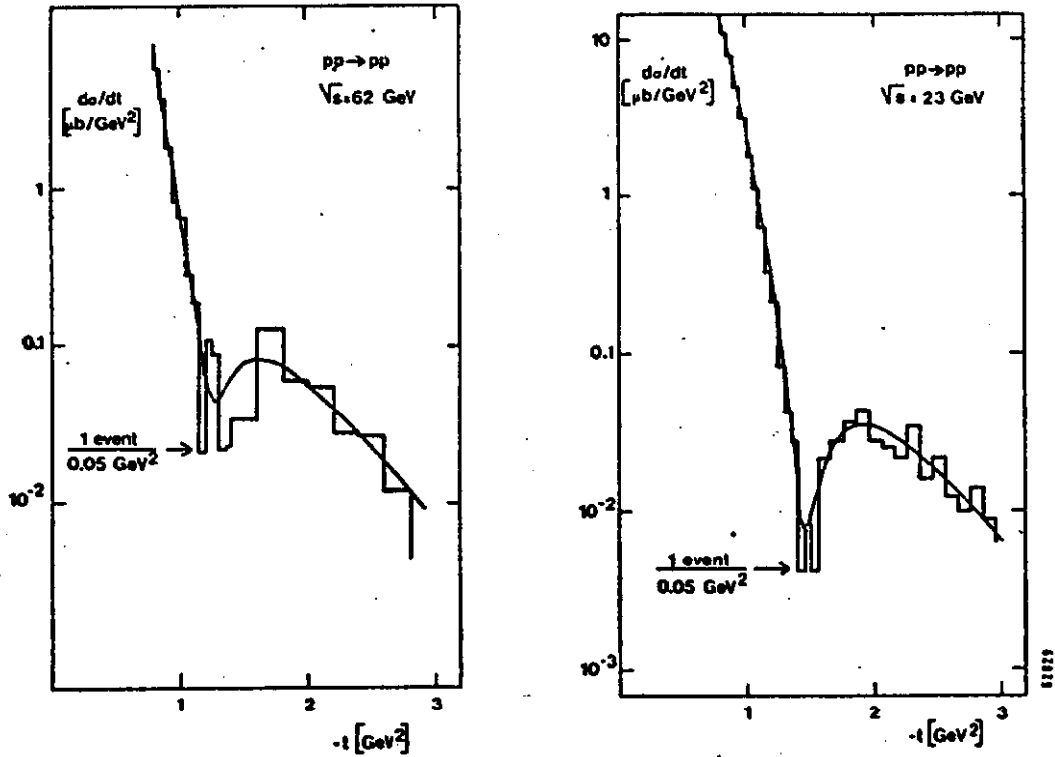


Fig. 3.4. Large angle elastic scattering data at $\sqrt{s} = 23$ and 62 GeV (74-13). The curves represent four-parameter fits according to Eq. (3.2). The data have a normalization uncertainty of $\pm 20\%$.

1.3 (GeV/c)^2 at $\sqrt{s} = 62$ GeV. The height of the maximum is instead increasing with energy.

The inward moving of the dip and the increasing of the secondary maximum, may come about as the result of an interference effect of a shrinking small $-t$ amplitude with a large $-t$ amplitude which is energy independent.

The integration of the differential cross section yields the total elastic cross section (which is approximately equal to $\sigma_{el} \simeq \sigma_{tot}^2/b$). The inelastic cross section is then given by $\sigma_{in} = \sigma_{tot} - \sigma_{el}$. Both σ_{el} and σ_{in} rise in the ISR energy range, with σ_{el} rising probably more than σ_{tot} (Fig. 3.6).

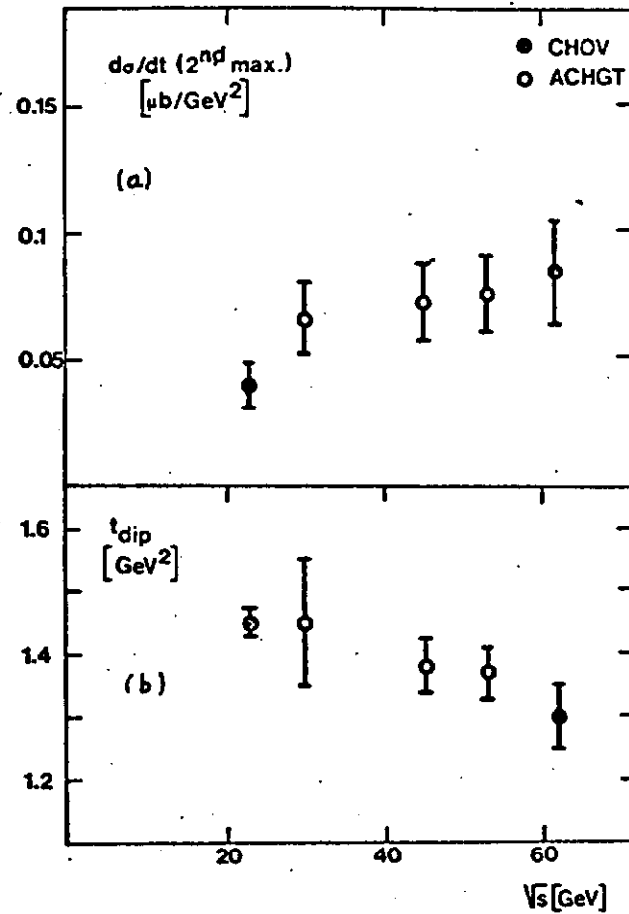


Fig. 3.5. (a) Height of the second maximum in pp elastic scattering as a function of energy.

(b) Position of the minimum near $|t| \sim 1.4 (\text{GeV}/c)^2$ as a function of energy.

Many models have been proposed to explain the shape of the pp elastic scattering differential cross section at ISR energies. Some geometrical models picture the proton as made of an inner core, which expands as the energy increases, and of an outer layer of constant thickness. Figure 3.7 shows the opaqueness of the proton at the two extreme ISR energies.

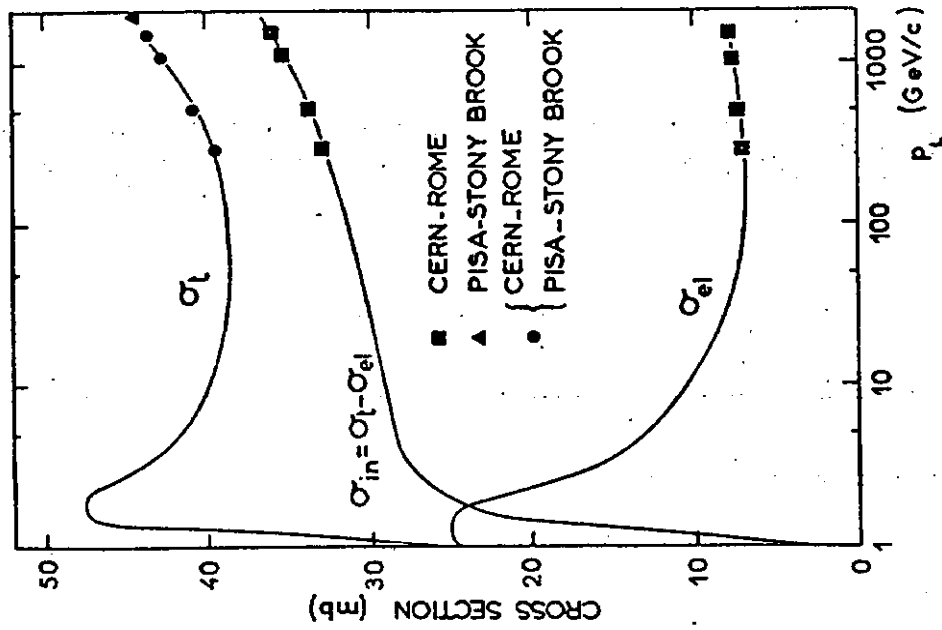


Fig. 3.6. Total, inelastic and elastic proton-proton cross sections versus laboratory momentum.

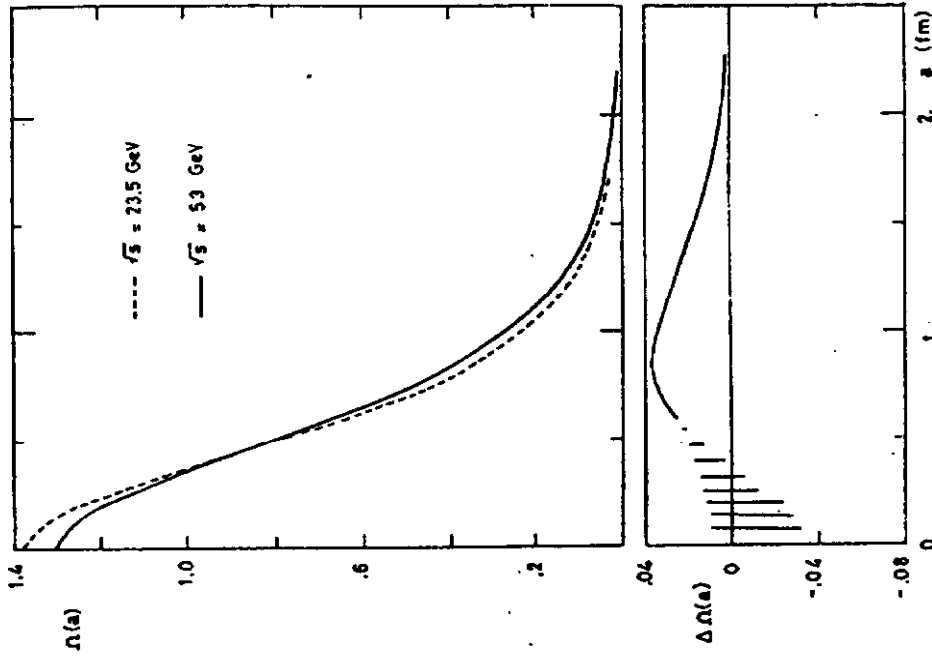


Fig. 3.7. Proton-proton opacity as a function of the impact parameter at the two extreme ISR energies. The opacity is computed from the differential cross section using a Fourier transform. The lower part of the figure shows the increment of the opacity in the ISR energy range (from U. Amaldi).

4. SINGLE-INCLUSIVE REACTIONS

Inclusive reactions of order one, defined as those reactions where one observes only one particle in the final state

$$a + b \rightarrow c + X, \quad (4.1)$$

have been studied with single arm spectrometers, with particle identification detectors. If particles a and b are protons and c is a proton going in the forward direction, one speaks of c as a leading particle. In all the other cases particle c is a produced particle.

We shall use the following independent variables

Total c.m. energy squared

$$s = (p_a + p_b)^2 = E_{cm}^2 \quad (4.2)$$

Transverse momentum of c

$$p_t = p \sin \theta = p_{clab} \sin \theta_{clab} \quad (4.3)$$

Longitudinal c.m. momentum of c

$$p_l = p \cos \theta \quad (4.4)$$

Feynman x variable

$$x = \frac{p_l}{p_{lmax}} \stackrel{s \gg}{\approx} \frac{2p_l}{\sqrt{s}} \quad (4.5a)$$

Transverse x

$$x_t = \frac{2p_t}{\sqrt{s}} \quad (4.5b)$$

x_R

$$x_R = \sqrt{x^2 + x_t^2} \quad (4.5c)$$

c.m. rapidity variable

$$y = \frac{1}{2} \ln \frac{E + p_\ell}{E - p_\ell} \xrightarrow[p_t^2 > m_c^2]{} - \ln \operatorname{tg} \frac{\theta}{2} \quad (4.6)$$

laboratory rapidity

$$y_{\text{lab}} = y_{\text{ac}} = y_a - y_c \quad (4.7)$$

missing mass

$$M^2 = E_x^2 - p_x^2 = (p_a + p_b - p_c)^2 \quad (4.8)$$

if $a = b = c = p$

$$M^2 = s + m_p^2 - 2\sqrt{s} E_c \quad (4.9)$$

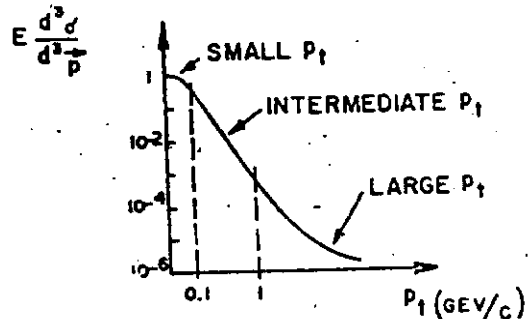
For the differential one-particle inclusive cross section we shall use the invariant form

$$f = f(s, p_t, y) = E \frac{d^3\sigma}{d^3\vec{p}} = \frac{E}{p} \frac{d^2\sigma}{d\Omega dp} = \frac{E}{\pi} \frac{d^2\sigma}{dp_\ell dp_t} = \frac{1}{\pi} \frac{d^2\sigma}{dy dp_t^2} = \frac{s}{\pi} \frac{d^2\sigma}{dt dM^2} \quad (4.10)$$

Most results on single inclusive reactions at the ISR became available some time ago; recent new results complete the general picture. We shall attempt to make a sketchy overall view of the results discussing the behavior of the invariant cross section as function of one variable at a time keeping the other two fixed. We shall then discuss general features, like multiplicities and average transverse momenta.

$$4.1. \quad f = f(p_t)$$

The general appearance of the invariant cross section as a function of p_t is sketched here. The bulk of the experimental data concerns the intermediate p_t -region, which may be



defined as $0.1 < p_t < 1$ GeV/c. At the ISR there are no data in the low p_t -region ($p_t < 0.1$ GeV/c). Fig. 4.1 shows the transverse momentum distribution at fixed values of the laboratory rapidity, y_{lab} , for pion production in the fragmentation region (74-4). The distributions are well represented by an exponential function in p_t .

$$f = E \frac{d^2\sigma}{d^3p} = A \exp(-Bp_t) \quad (4.11)$$

This is true for the production of any particle in both fragmentation and central regions, with the exception of protons, whose distributions are best represented with exponential functions at small values of x and by gaussian functions at large values of x .

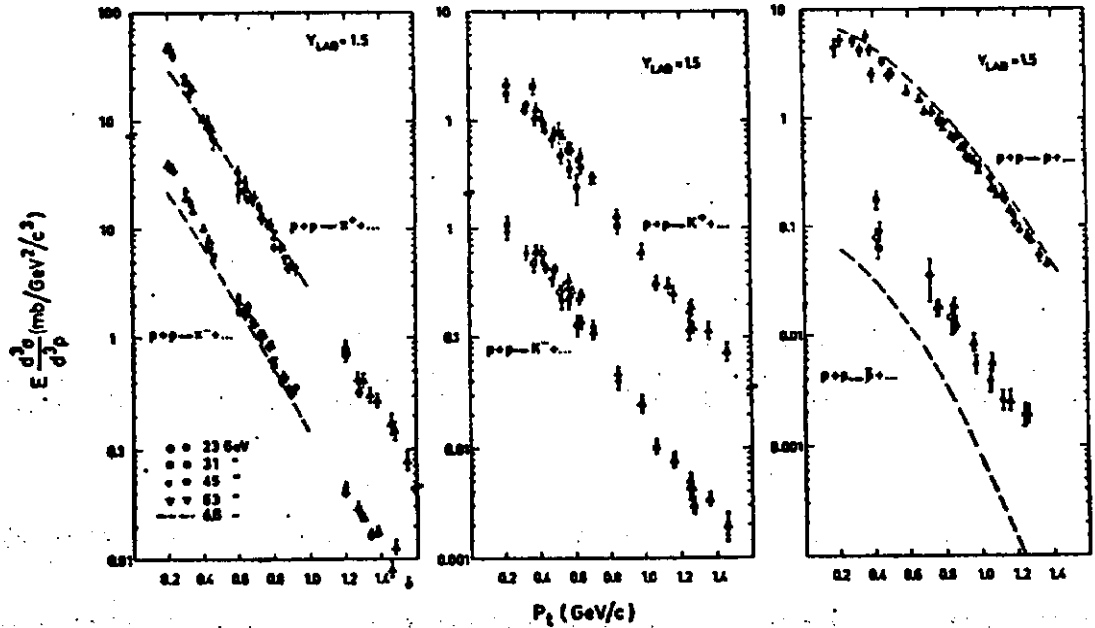


Fig. 4.1. The invariant cross sections for the production of π^\pm , K^\pm , p and \bar{p} plotted versus transverse momentum at a value $y_{lab} = 1.5$ (74-4).

The $f = f(p_t)$ distributions are better represented by exponentials when the data refer to $y_{lab} = \text{const}$ than when $x = \text{const}$. The slopes are larger for pions [slope $B \simeq 6.8 (\text{GeV}/c)^{-1}$]; smaller for kaons ($B_{K^+} \simeq B_{K^-} \simeq 5.0$) and still smaller for protons and antiprotons ($B_p \simeq B_{\bar{p}} \simeq 4$). The π^+ slope is just a little smaller than that of π^- ($B_{\pi^+} \simeq 6.5$, $B_{\pi^-} \simeq 7$).

In the large p_t -region ($p_t > 1 \text{ GeV}/c$), the invariant sections decrease less fast than an exponential and have a stronger energy dependence than at lower transverse momenta. The large p_t 's will be studied separately in Section 7.

4.1.1. Average transverse momentum

The average transverse momentum for the production of particle c may be defined as

$$\langle p_t \rangle_{y_{lab}} = \frac{\int p_t f(p_t, y_{lab} = \text{const}) dp_t^2}{\int f(p_t, y_{lab} = \text{const}) dp_t^2} \quad (4.12)$$

where the subscript y_{lab} means that the computation was performed using invariant cross sections at fixed values of y_{lab} .

The practical computation of the average transverse momentum may be performed using directly the definition (4.12). If the cross section is exponential in p_t one has simply

$$\langle p_t \rangle_y \simeq \frac{\int p_t e^{-B p_t} dp_t^2}{\int e^{-B p_t} dp_t^2} = \frac{2}{B} \quad (4.13)$$

Since there are few data for $p_t < 0.1 \text{ GeV}/c$ (low p_t -region) and $p_t > 1.5 \text{ GeV}/c$, one needs extrapolations of the cross sections in order to compute the average values of the transverse momentum for different particles. The average value of the transverse momentum is essentially determined by data in the intermediate region; thus the error introduced by the extrapolations

is small. It may be estimated to be between 5-10%, arising mainly from uncertainties in the low p_t -region.

Figure 4.2 shows the average values of the transverse momentum for π^\pm , K^\pm , p , and \bar{p} computed for fixed values of y_{lab} plotted versus y_{lab} (74-4). It leads to the following picture for pion production.

- (i) For small y_{lab} , $\langle p_t \rangle_{y_{lab}}$ is very small and increases quickly. This rapid change for $y_{lab} < 1$ is a kinematical effect, since in this region one simply cannot produce large transverse momenta. For $y_{lab} > 2$, $\langle p_t \rangle_{y_{lab}}$ increases slowly with y_{lab} . This means that the factorization of the invariant cross section in terms of p_t and y_{lab} [$f(p_t, y_{lab}) = g(p_t) h(y_{lab})$] is only an approximation valid to 5-10%.

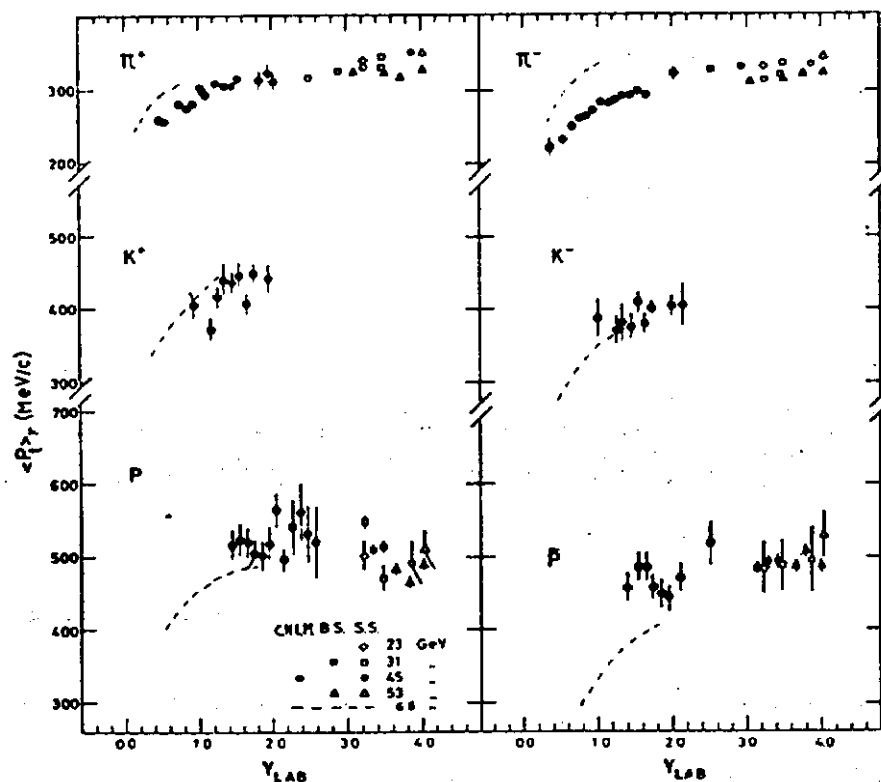


Fig. 4.2. Average values of the transverse momentum for π^+ , π^- , K^+ , K^- , p and \bar{p} production, computed at fixed values of the y_{lab} variable, plotted versus y_{lab} (74-4).

- (ii) The shapes of the $\langle p_t \rangle_{\pi^+, y_{lab}}$ and $\langle p_t \rangle_{\pi^-, y_{lab}}$ are quite similar, the π^+ 's having a slightly larger value of the average transverse momentum.
- (iii) The results from different energies superimpose one on the other on a kind of "universal curve," which may be explored completely only at the highest energies. If this is correct, it is clear that the integration of $\langle p_t \rangle_{y_{lab}}$ over y_{lab} will yield average values which increase slowly with energy (this will be discussed in more detail later).

Within their larger errors, the average transverse momentum of kaons behaves as for pions, but the "plateau" is at about 450 and 400 MeV/c for K^+ and K^- respectively.

For protons and antiprotons the average transverse momentum is about 500 MeV/c.

4.2. $f = f(y_{lab})$; $f = f(x)$

A compilation of data for the production of π^\pm , K^\pm , p and \bar{p} at different ISR energies and fixed value of $p_t = 0.4$ GeV/c is shown in Fig. 4.3 versus laboratory rapidity (74-23). The dotted lines represent interpolations through data at a laboratory momentum of 24 GeV/c.

The shape of $f = f(y_{lab})$ at fixed p_t is essentially the same for π^\pm , K^\pm and \bar{p} . The cross section is small at small values of y_{lab} ; it grows with y_{lab} , until when it reaches a kind of a plateau for $y_{lab} > 2$. In reality the plateau is slowly rising with y_{lab} , by about 10% in two units of rapidity. This means that the scaling region has not quite been reached even at the highest ISR energies. Only the protons have a different shape, which reflects their leading particle nature. All the ISR data taken at different energies superimpose on the same curve; the data at the laboratory momentum of 24 GeV/c are considerably lower for \bar{p} , just a little bit lower for K^- and just a little

higher for protons. This emphasizes the different ways in which the scaling region is reached, though the variations are modest when the data are plotted versus y_{lab} .

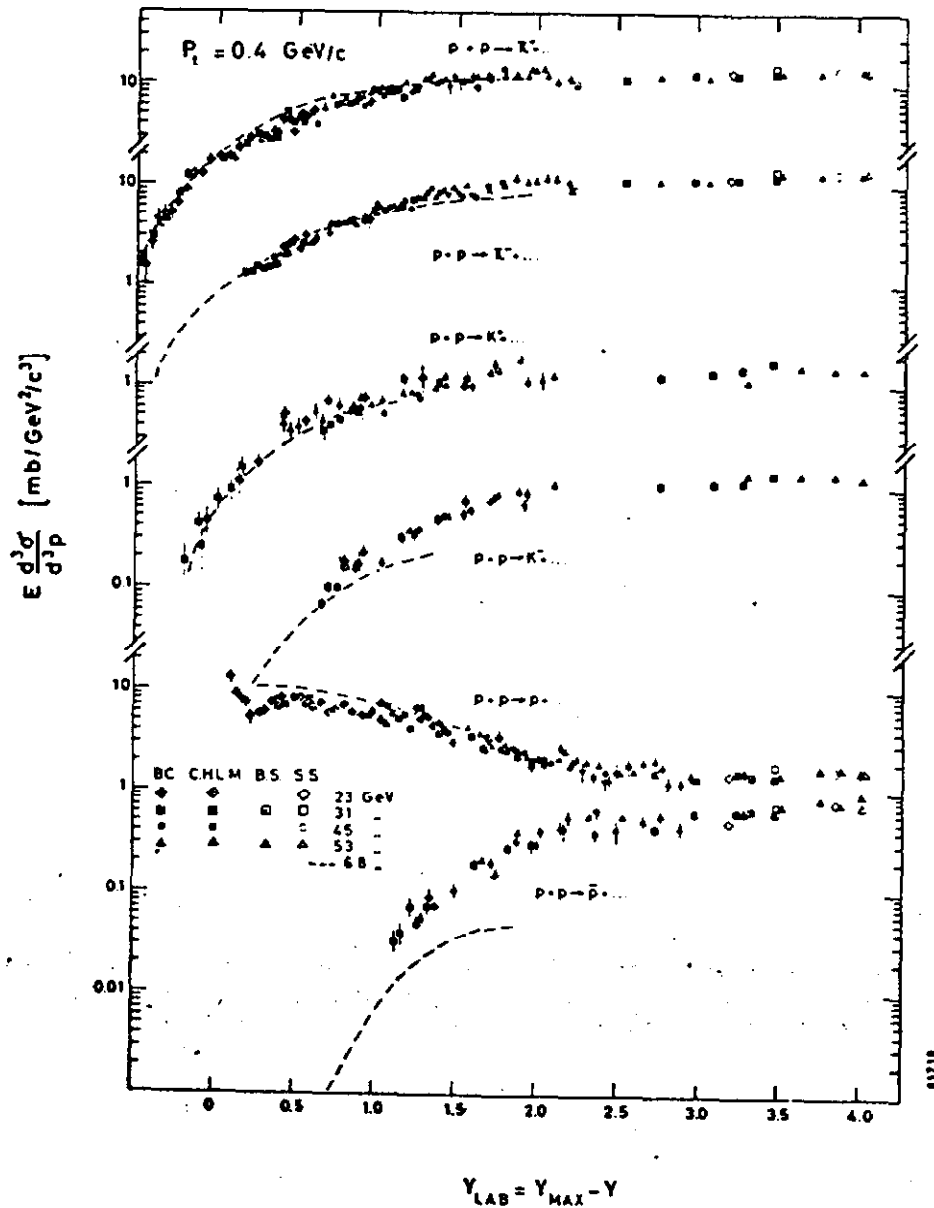


Fig. 4.3. The invariant cross sections for pion, kaon, proton and antiproton production at $p_t = 0.4 \text{ GeV}/c$ plotted versus y_{lab} . The ISR data are from references 74-4, 74-25, 72-12, 73-13, 73-14, 73-14 and 72-11. The dashed lines refer to data at 24 GeV/c.

In terms of the rapidity variable it is easy to separate the fragmentation ($y_{\text{lab}} < 2$) and central regions ($y_{\text{lab}} > 2$). It is not so easy for other variables, like the x -variable. On the other hand one may learn some other details when the data are plotted as function of x . An illustration of $f = f(x)$ at $\sqrt{s} = 53 \text{ GeV}$ and $p_t = 0.4 \text{ GeV/c}$ for the production of various particles is sketched in Fig. 4.4.

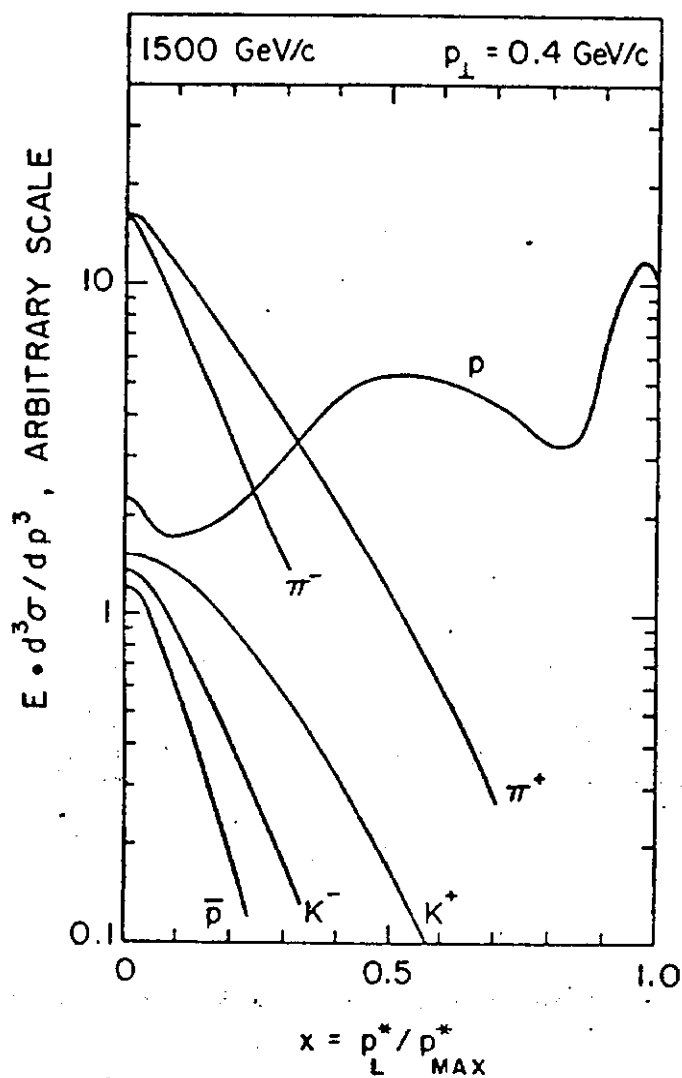


Fig. 4.4. The invariant cross-sections for the production of various particles at $p_t = 0.4 \text{ GeV/c}$, plotted versus x . The vertical arbitrary scale is in reality very close to mb/GeV^2 (from D.R.O. Morrison).

Figure 4.5 shows a compilation of particle ratios: note that particle to antiparticle ratios tend to 1 when y_{lab} increases.

4.3. $f = f(s)$

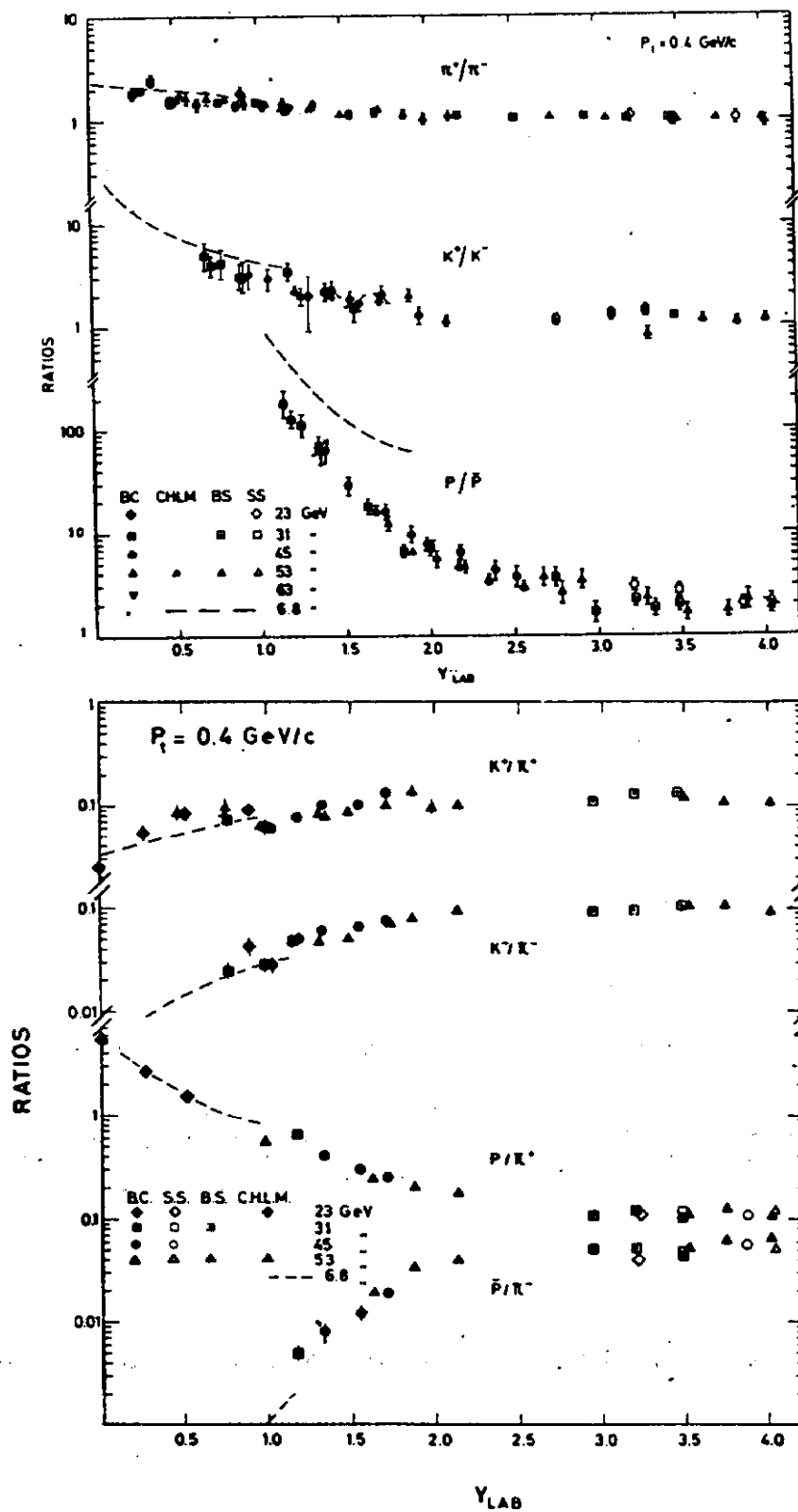
The energy dependence of a collection of invariant cross sections at fixed values of (x, p_t) is shown in Fig. 4.6 (74-30). The data in the figure come from a variety of experiments, using a variety of experimental techniques. Therefore also their systematic uncertainties have to be considered. This means that no cross section is known with an accuracy of better than $\pm 10\%$.

The energy dependence of the invariant cross sections may be parametrized with expressions of the form

$$f = E \frac{d^3\sigma}{d^3p} = A + Bs^{-\alpha} \quad (4.14)$$

Several models of particle production predicted an energy dependence (4.14) with $\alpha = 1/2$ for data in the fragmentation region and $\alpha = 1/4$ in the central region. Table 4.1 gives the results of least squares fits to the available data to formula (4.14) with $\alpha = 1/2$ and $\alpha = 1/4$. When systematic errors are included, the chi squares are reasonable, but both forms are compatible with the data.

From the figures and from the analysis of the fits one sees immediately that a kind of asymptotic region, where there is only a minor energy dependence, is attained at lower energies for positive particles than for negative ones. Moreover there is a hierarchy connected with the mass of the particles produced: the scaling region for instance is attained first by pions, then by kaons, while the antiproton cross section is still increasing considerably in the ISR energy range. The whole study of energy dependence is moreover strongly coupled with the choice of independent variables.



61699

Fig. 4.5. Particle ratios at a value of $p_t = 0.4 \text{ GeV/c}$ plotted versus y_{lab} (74-23).

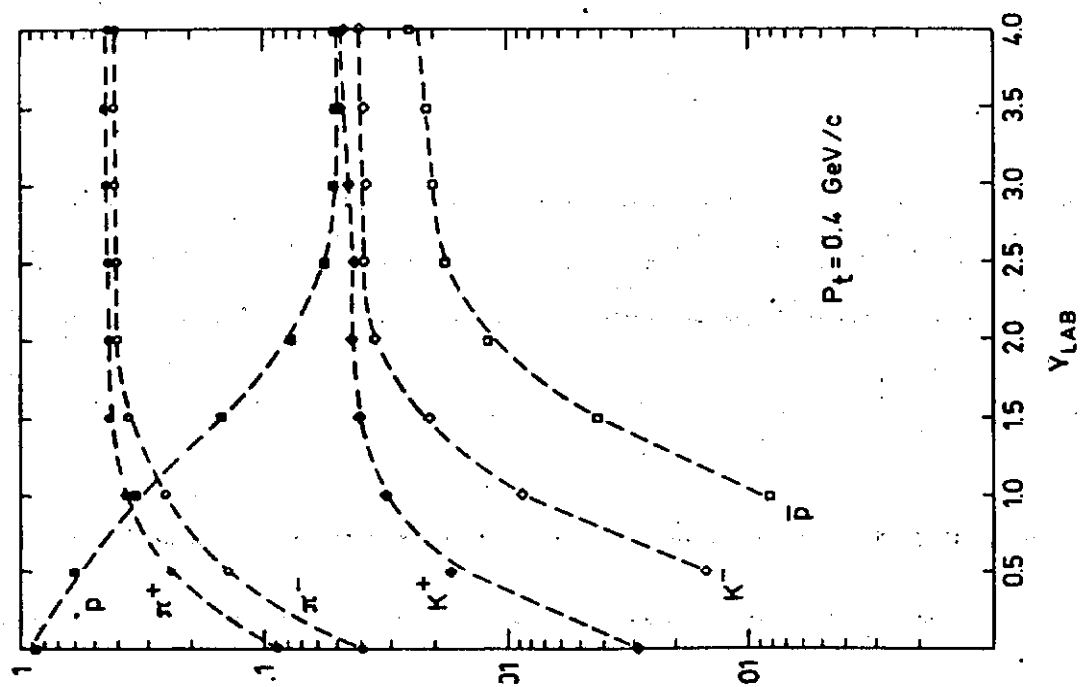
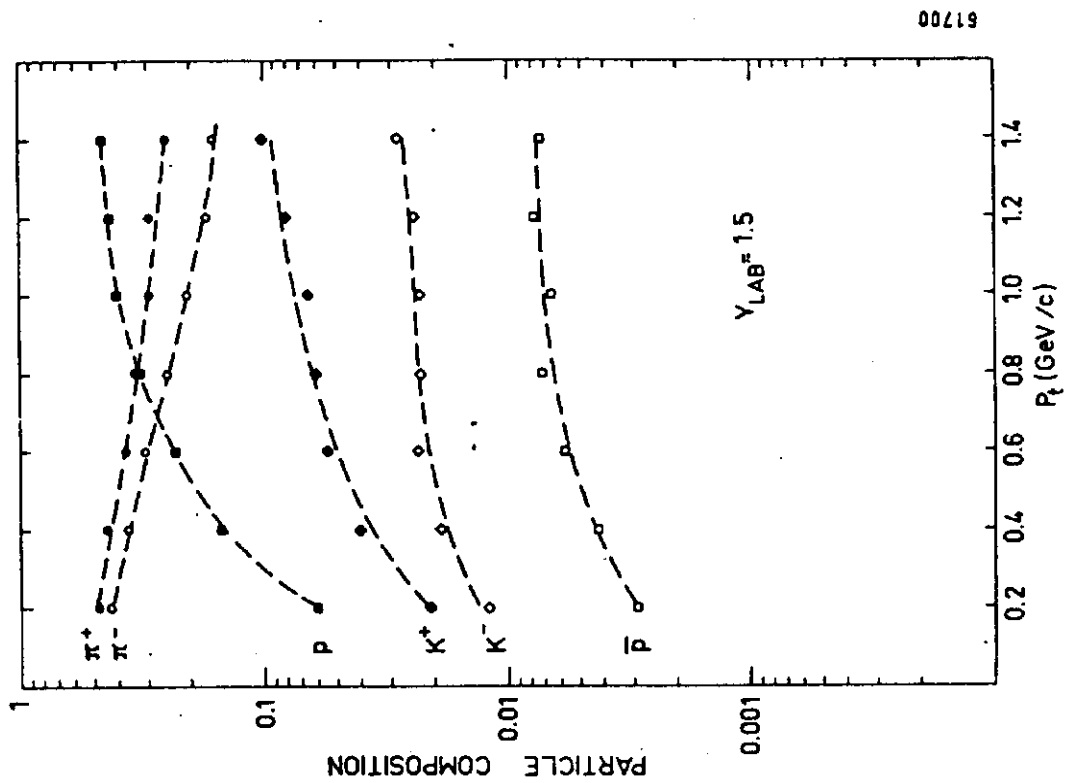


Fig. 6.3

TABLE 4.1

Results of Fitting the Invariant Cross Sections at Fixed (x, p_t) for π^+ Production to Formula (4.14)
 with $\alpha = 1/4$ and $\alpha = 1/2$ (R202, 74-30)

x	p_t	$A + Bs^{-1/2}$				$A + Bs^{-1/4}$			
		A	B	χ^2/ND	A	B	χ^2/ND	A	χ^2/ND
0.0	0.35	20.1 ± 0.8	-30.9 ± 5.1	0.14	22.7 ± 1.2	-20.2 ± 3.4	0.36		
	0.40	14.3 ± 0.5	-19.7 ± 3.8	0.55	15.7 ± 0.7	-11.5 ± 2.3	0.68		
	0.50	7.9 ± 0.4	-10.3 ± 2.8	0.15	8.7 ± 0.5	-6.2 ± 1.7	0.11		
	0.60	3.92 ± 0.18	-3.46 ± 1.50	1.26	4.16 ± 0.27	-2.03 ± 0.88	1.27		
0.16	0.35	11.0 ± 0.6	-6.6 ± 4.1	0.42	11.5 ± 0.9	-4.1 ± 2.6	0.43		
	0.40	8.3 ± 0.4	-4.9 ± 3.0	0.31	8.7 ± 0.6	-3.0 ± 1.8	0.32		
	0.50	5.60 ± 0.38	-8.4 ± 2.5	0.40	6.2 ± 0.5	-5.0 ± 1.5	0.35		
	0.60	2.94 ± 0.21	-2.7 ± 1.4	1.44	3.13 ± 0.31	-1.60 ± 0.83	1.45		

4.4. Multiplicities

The multiplicity of particle c is defined as the average number of particles c produced per interaction. At the ISR the multiplicities have to be computed by integration of single particle spectra in inclusive reactions:

$$\langle n_c \rangle = \frac{1}{\sigma_{in}} \int f \frac{d^3p}{E} \quad (4.15)$$

If factorization in (p_t, y_{lab}) holds the computation of (4.15) becomes particularly simple:

$$f(y, p_t) \simeq g(y) h(p_t) \simeq G(y) \exp(-B p_t) \quad (4.16)$$

from which

$$\langle n_c \rangle \simeq \frac{\pi}{\sigma_{in}} \int_0^\infty [\exp -B p_t] dp_t^2 \int_{y_{min}}^{y_{max}} G(y) dy \simeq \frac{4\pi}{\sigma_{in} B^2} \int_0^{y_{max}} G(y) dy \quad (4.17)$$

We know that the average transverse momentum changes with y_{lab} and that $f = f(y_{lab})$ is not constant, particularly at small y_{lab} . Thus Eq. (4.17) is not exact; however, it may still be used as an empirical formula and still yields reasonable results. Since the y_{lab} distributions at $p_t = 0$ are not known, one uses those at $p_t = 0.4$ GeV/c:

$$\langle n_c \rangle \simeq \frac{4\pi}{\sigma_{in} B^2} \int_0^{y_{max}} \frac{f(y, p_t = 0.4)}{\exp(-0.4B)} dy \quad (4.18)$$

The integral in (4.18) was computed numerically, using values of σ_{in} slowly increasing with energy.

The multiplicities of π^- , π^+ , K^- , K^+ , \bar{p} , p , and the total charged multiplicity are shown in Fig. 4.7 as a function of s (73-20, 74-35).

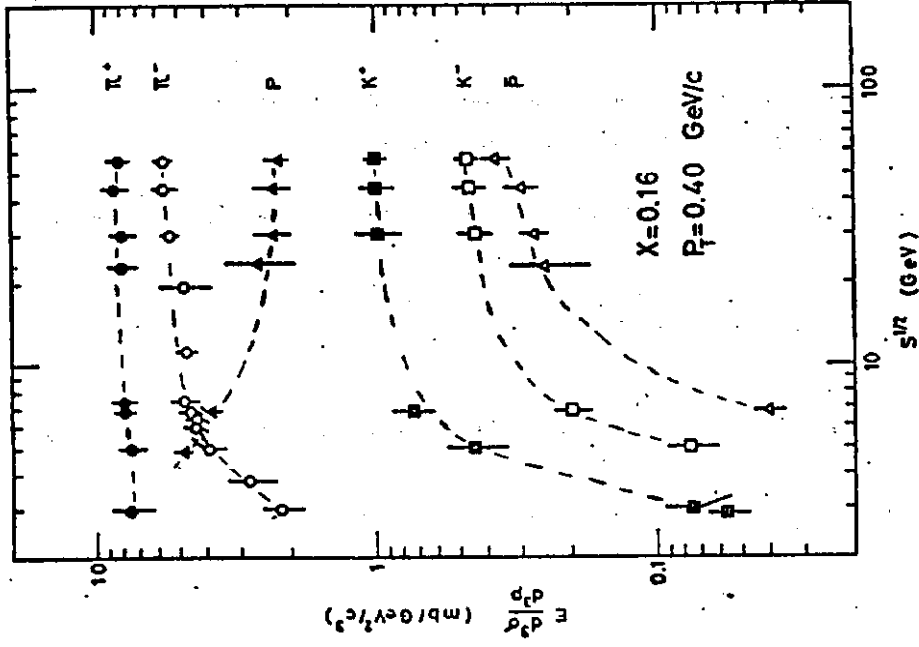


Fig. 4.6. The invariant cross sections for the production of π^\pm , K^\pm , p and \bar{p} at $x = 0.16$ and $P_T = 0.4$ GeV/c plotted versus \sqrt{s} (74-34).

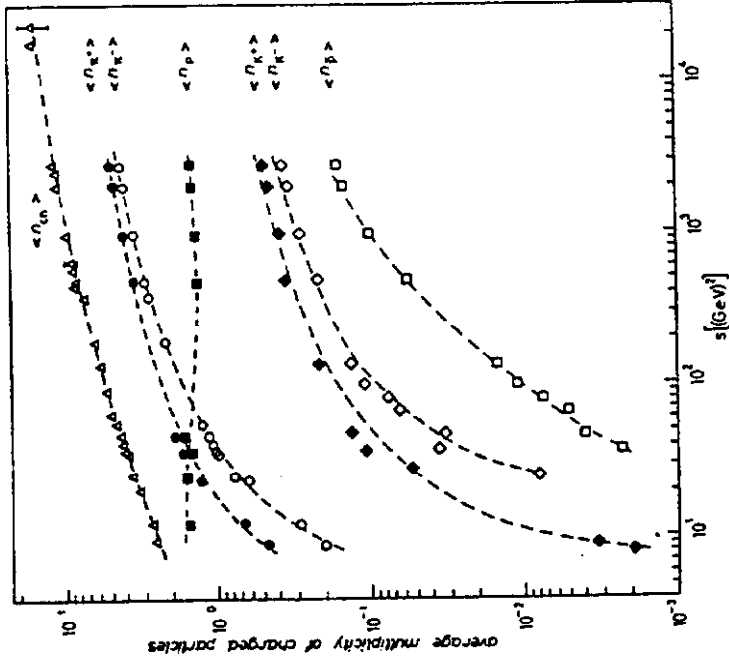


Fig. 4.7. The average multiplicities of π^\pm , K^\pm , p , \bar{p} and for the sum of the six charged particles, plotted versus s . The dashed lines represent the results of the fits according to Eq. 4.19 (74-30).

The energy dependence of the multiplicities may be fitted with formulae of the type:

$$\langle n_i \rangle = A + B \ln s + C s^{-1/2} \quad (4.19)$$

$$\langle n_i \rangle = A' + B' \ln s + C' s^{-1/2} \ln s \quad (4.20)$$

In general the fits according to Eq. (4.19) yield lower χ^2 than those according to (4.20). The proton multiplicity has only a very minor energy dependence.

The average multiplicity $\langle n_{\pi^+} \rangle$ is larger than $\langle n_{\pi^-} \rangle$, the difference being approximately constant with energy ($\langle n_{\pi^+} \rangle - \langle n_{\pi^-} \rangle = 0.5$). Thus the percentage difference is decreasing with increasing energy. The same trend is valid also for K^+ and K^- . The ratio of kaon to pion multiplicities increases with increasing energy and reaches an approximately constant value at ISR energies.

4.5. Energy Dependence of the Average Transverse Momentum

For each produced particle, c , the average transverse momentum integrated over the y_{lab} variable is obtained by integrating (4.12) or (4.13):

$$\langle p_t \rangle_c = \frac{\int p_t f d^3p/E}{\int f d^3p/E} = \frac{\int [\langle p_t \rangle_{y_{lab}} \int f dp_t^2] dy_{lab}}{\int [\int f dp_t^2] dy_{lab}} \quad (4.21)$$

$$\approx \frac{\int_{y_{min}}^{y_{max}} \langle p_t \rangle_{y_{lab}} f(y_{lab}, p_t = 0.4) dy_{lab}}{\int_{y_{min}}^{y_{max}} f(y_{lab}, p_t = 0.4) dy_{lab}} \quad (4.22)$$

Formula (4.22) is an approximation which uses the data at $p_t = 0.4$ GeV/c, the values $\langle p_t \rangle_{y_{lab}}$ and assumes factorization of the cross section in (y_{lab}, p_t) .

The computation of the average transverse momenta at different energies is considerably simplified if one assumes that there are "universal" curves for $f(y_{\text{lab}}, p_t = 0.4)$ and $\langle p_t \rangle_{y_{\text{lab}}}$; that is, curves on which data at different energies always lie. This seems to be true for laboratory momenta above 10-20 GeV/c.

The results of the computations for the average transverse momenta are shown in Fig. 4.8, which give also the average transverse momentum for the production of all the charged particles, defined as

$$\begin{aligned} \langle p_t \rangle_{\text{charged}} &= \left[\langle n_{\pi^+} \rangle \langle p_t \rangle_{\pi^+} + \langle n_{\pi^-} \rangle \langle p_t \rangle_{\pi^-} + \langle n_{K^+} \rangle \langle p_t \rangle_{K^+} + \langle n_{K^-} \rangle \langle p_t \rangle_{K^-} + \langle n_p \rangle \langle p_t \rangle_p \right. \\ &\quad \left. + \langle n_{\bar{p}} \rangle \langle p_t \rangle_{\bar{p}} \right] \frac{1}{n_{\text{charged}}} \end{aligned} \quad (4.23)$$

where $\langle n_i \rangle$ and $\langle n_{\text{charged}} \rangle$ are the average multiplicities for the production of particle i and the average charged multiplicity, respectively. Because of the lack of precise data at small y_{lab} , only an estimate of the $\langle p_t \rangle_p$ has been made.

The absolute values of the average transverse momenta may have errors of the order of 10% arising mainly from uncertainties of the data at low and high p_t and from the assumption of the universal curves used. On the other hand, the point-to-point errors and the error of, say, the π^+ curve with respect to the π^- curve are expected to be of a few per cent.

Within errors all the average transverse momenta increase very slowly with primary energy. This is in contradiction with some very high energy cosmic ray data presented at the London Conference.

As far as the relations between the $\langle p_t \rangle$ for different particles are concerned, one may notice that the average p_t for positive particles is a little larger than for the corresponding negative ones ($\langle p_t \rangle_{\pi^+} \gtrsim \langle p_t \rangle_{\pi^-}$ and $\langle p_t \rangle_{K^+} \gtrsim \langle p_t \rangle_{K^-}$) and that the average p_t increases with the mass of the produced particle.

Among the various theoretical models which are capable of predicting the average values of the transverse momentum, there is the thermodynamic model of Hagedorn et al. in which the average transverse momentum has a simple meaning. It is connected with the temperature of the "fireball," or "fireballs," produced by the merging of the two incidence protons, from which come the produced particle. In a naive way, one may think of the fireball as a "liquid drop at the boiling point" from which "evaporate" the various particles. Increasing the energy inside the drop does not result in an increase of its temperature nor of the average transverse momentum of the produced particles; but the average number of produced particles increases. The model predicts the following relation between average transverse momentum and temperature:

$$\langle p_t(m,T) \rangle \simeq \sqrt{\frac{mT}{2}} \frac{K_{5/2}(m/T)}{K_2(m/T)} \quad (4.24)$$

where $K_{5/2}$ and K_2 are Hankel's functions and m is the mass of the produced particles. The vertical scale on the right hand side of Fig. 4.8 gives the temperatures for each produced particle computed with Eq. (4.24). The energy dependence of the temperatures is weak as anticipated. The temperatures corresponding to the different particles are almost equal. One may say that all the particles are produced from a region at the same temperature, or that

$$T_{\pi^-} \simeq T_{\pi^+} \simeq T_{K^-} < T_{K^+} < T_{\bar{p}}.$$

5. CORRELATIONS

The study of correlations between the final state particles produced in proton proton collisions offers a very wide field of research which is being attacked by a growing number of groups at the ISR. Measurements of correlation functions have been suggested by many authors as a means of discriminating among different models of particle production. They could for instance discriminate between models in which the observed particles are the

decay products of heavier objects and models where the observed particles are directly produced. Most of the correlations are studied in inclusive reactions of order 2, that is

$$p + p \rightarrow c_1 + c_2 + \text{anything} \quad (5.1)$$

where "anything" is either not observed or only observed in so far as some features only, like the number of tracks.

The number of independent variables in reaction (5.1) is large:

$$\begin{aligned} & s; p_{t1}, y_1, \phi_1; p_{t2}, y_2, \phi_2; \\ & \text{nature of } c_1, c_2; \\ & \text{some feature of the "anything"} \end{aligned} \quad (5.2)$$

that is total c.m. energy, nature of the two observed particles and three kinematics variables for each observed particle (for instance p_t , rapidity and azimuthal angle, or other equivalent variables). One azimuthal angle is ignorable, because the initial protons are unpolarized.

The number of correlations one can study is thus very large: one may study correlations in polar angles, in azimuth, in momentum and mixed or more complex correlations. For each of these one can then investigate their dependence in energy, types of observed particles, on the kinematical regions of one particle, on the observed multiplicity, etc.

From the experimental point of view one has to point out that besides experiments using layouts specifically designed for the study of certain correlations, there are others where some equipment was added to an existing apparatus, for instance some scintillation counters to a single arm spectrometer.

The best layout for studying reaction (5.1) would consist of a two-arm spectrometer with particle identification. At the ISR there are only three such systems (in I1 the Saclay spectrometer, in I2 the combination of the small angle and large angle spectrometers, in I6 the layout used for elastic scattering measurements). All other layouts do not have complete particle identification.

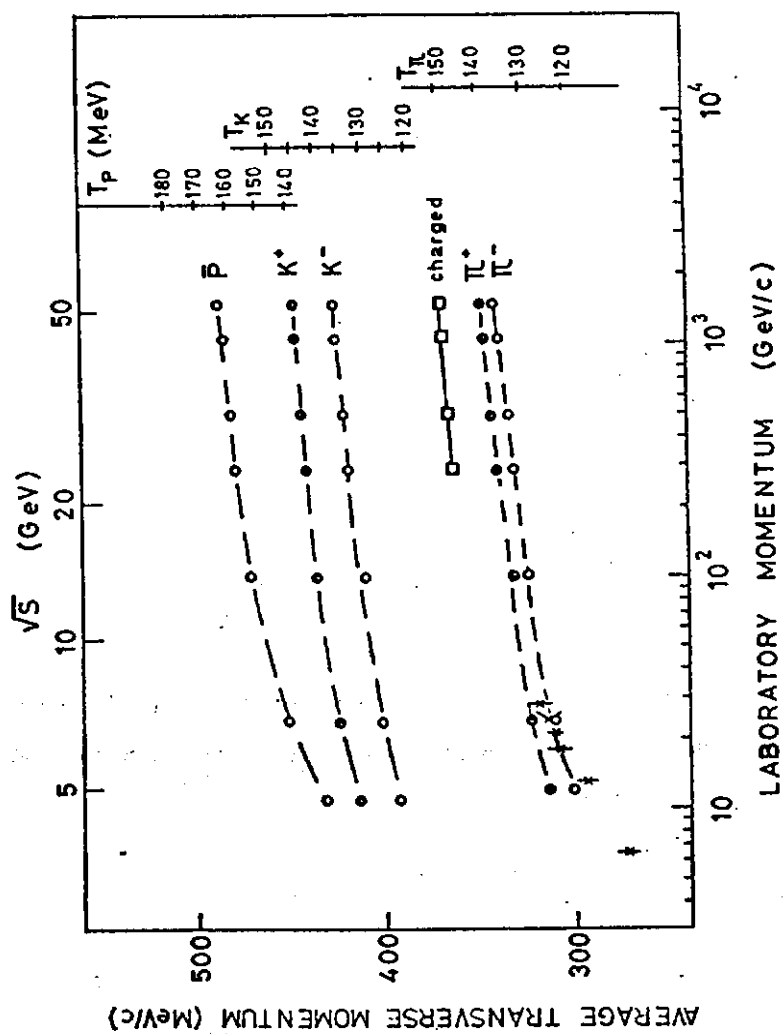


Fig. 4.8. Average transverse momenta for the production of pions, kaons, antiprotons and all charged particles plotted versus the laboratory momentum. On the right hand side are shown "temperature" scales for different particles, computed with formula (4.24) (74-30)

The conservation of energy and momentum produces automatically some sort of correlations among the particles in the final state. One has to remove these "kinematical" effects before being able to study the dynamics of the process observed.

In the following we shall schematize the measured correlations in (i) rapidity, (ii) azimuth, (iii) transverse momentum, and (iv) more complex ones, like correlations with a fast forward particle. Correlations involving diffractive protons and particles with large transverse momentum will be discussed separately.

Figure 5.1 is a sketch of the layouts used at the ISR to measure correlations.

5.1. Rapidity Correlations

We shall define the single particle density distribution for reaction (4.1) as:

$$\rho^{(1)}(y) = \frac{1}{\sigma_{in}} \frac{d\sigma}{dy} \quad (5.3)$$

where σ_{in} is the inelastic cross section and $d\sigma/dy$ could be the result of integrations over p_t and ϕ . The two-particle density distribution for reaction (5.1) is defined as

$$\rho^{(2)}(y_1, y_2) = \frac{1}{\sigma_{in}} \frac{d^2\sigma}{dy_1 dy_2} \quad (5.4)$$

The rapidity correlation function will be defined as

$$\begin{aligned} R(y_1, y_2) &= \frac{\rho^{(2)}(y_1, y_2) - \rho^{(1)}(y_1) \rho^{(1)}(y_2)}{\rho^{(1)}(y_1) \rho^{(1)}(y_2)} \\ &= \frac{\sigma_{in} (d^2\sigma / dy_1 dy_2)}{(d\sigma/dy_1) (d\sigma/dy_2)} - 1 \end{aligned} \quad (5.5)$$

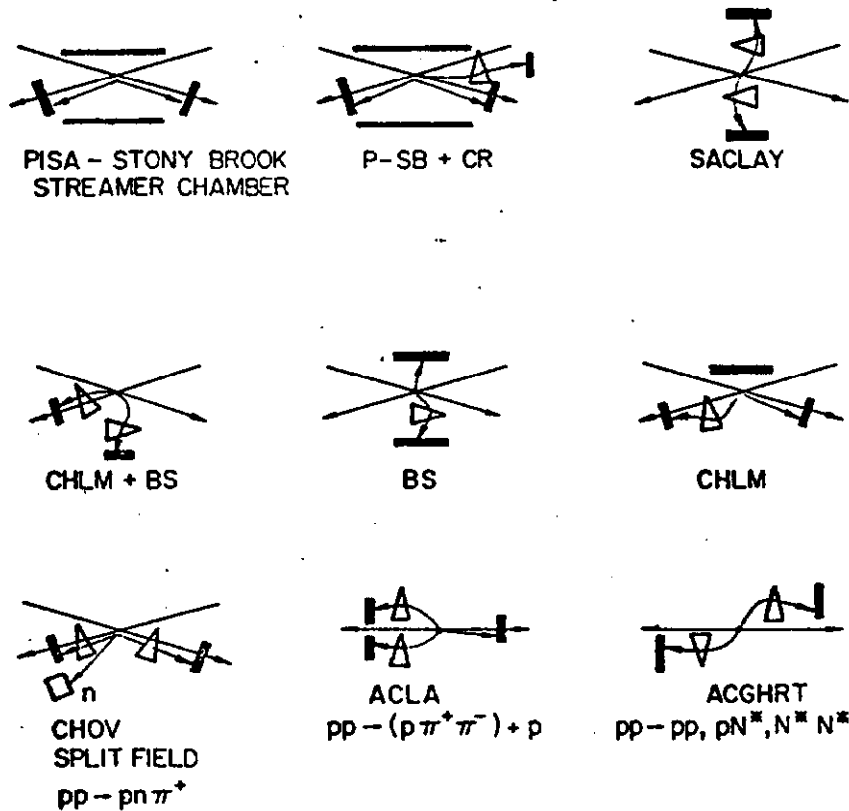


Fig. 5.1a

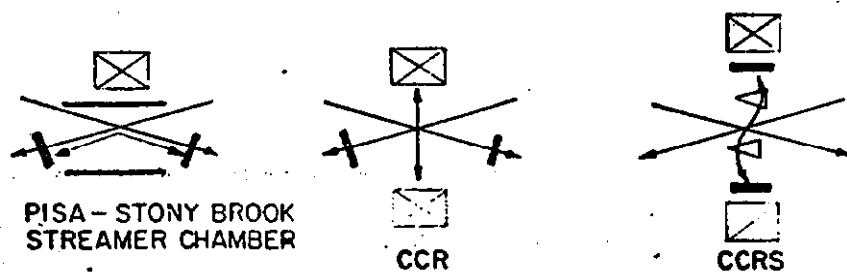


Fig. 5.1b

Fig. 5.1. Sketch of the correlations which have been studied at the ISR.
 (a) low p_t (b) large p_t . The ISR beams are shown as thin black lines, the triggering particles as outgoing lines (straight if there are no magnetic analysis, curved if there is). Magnets are indicated as prisms.

If particles c_1 and c_2 would be emitted independently, $\rho^{(2)}(y_1, y_2)$ would be the product of the two single particle distribution functions $\rho^{(1)}(y_1)$, $\rho^{(1)}(y_2)$ and $R(y_1, y_2)$ would be zero. Another type of correlation function is often quoted:

$$\begin{aligned} C(y_1, y_2) &= \rho^{(2)}(y_1, y_2) - \rho^{(1)}(y_1) \rho^{(1)}(y_2) \\ &= R(y_1, y_2) \rho^{(1)}(y_1) \rho^{(1)}(y_2) \end{aligned} \quad (5.6)$$

We shall discuss the rapidity correlations measured at the CERN-ISR by the Pisa-Stony Brook collaboration (74-1). They measured charged particle production, measuring only the angles of the produced particles with a counter hodoscope system. There is no knowledge of momenta nor of the sign or mass of the produced particle. From the knowledge of the angle θ one computes the variable

$$\eta = - \ln \operatorname{tg} \frac{\theta}{2} \quad (5.7)$$

which we shall call pseudorapidity; this is the rapidity for a particle of mass zero and is a good approximation of the rapidity for pions. The trigger requirement is such that (i) they accept about 92% of the inelastic collisions; (ii) they have a negligible contamination from elastic events; (iii) the minimum momentum detected is 80 MeV/c. The data have been corrected for γ -conversion, δ -rays, finite counter size, etc., and are integrated over the ϕ angles.

A qualitative description of the interactions was given by this collaboration selecting the events according to their multiplicity, removing the two tracks with the largest and smallest angles (i.e., pseudorapidities) and computing for the remaining tracks a mean pseudorapidity

$$\bar{\eta} = \frac{1}{n-2} \sum_i \eta_i \quad (5.8)$$

and a dispersion

$$\delta(\bar{\eta}) = \sqrt{\frac{\sum_i (\eta_i - \bar{\eta})^2}{n - 3}} \quad (5.9)$$

A three-dimensional plot of this data is shown in Fig. 5.2, where δ is plotted in the x-axis, $\bar{\eta}$ in the y-axis and the number of events in the z-axis. The plots are repeated as functions of event multiplicity at various ISR energies. At low multiplicities the graphs show two sharp peaks at large positive and negative values of η and relatively small values of δ . There is also a less prominent and broader bump centered around $\bar{\eta} \simeq 0$. The two narrow peaks at large $|\eta|$ become less prominent and eventually disappear at larger values of the multiplicity, while the converse is true for the broad peak at $\bar{\eta} \simeq 0$.

The two sharp peaks, prominent at low multiplicities, are interpreted as due to diffractive processes, while the broader bump, prominent at larger multiplicities, is interpreted as due to central processes. In a rapidity plot a diffractive event appears to have a large rapidity gap between one leading particle and the bulk of the others. A central process would lead to rapidity distributions with a larger average multiplicity, more uniformly distributed in rapidity (see Section 6.2).

This first analysis shows that there are correlations in rapidity and that they may be used together with the average multiplicity to classify the type of interactions.

Figure 5.3 shows the contours of constant $R(\eta_1, \eta_2)$ in the (η_1, η_2) plane at the two energies of $\sqrt{s} = 23$ and 63 GeV. Figure 5.4 shows $R(\eta_1, \eta_2)$ as function of η_1 for the fixed value of $\eta_2 = 0$. An analysis of these graphs yields the following conclusions:

- (i) The contours are symmetric about $\eta_1 = \eta_2$ (because of the definition (5.5)) and about $\eta_1 = -\eta_2$ (which was imposed in the fit as it should be for a symmetric pp system).
- (ii) For $|\eta_1|, |\eta_2| \leq 2$ (central region) the contours are nearly straight lines parallel to $\eta_1 = \eta_2$. Thus here the primary dependence of

PISA STONY BROOK

31.4-31.6 GeV/c

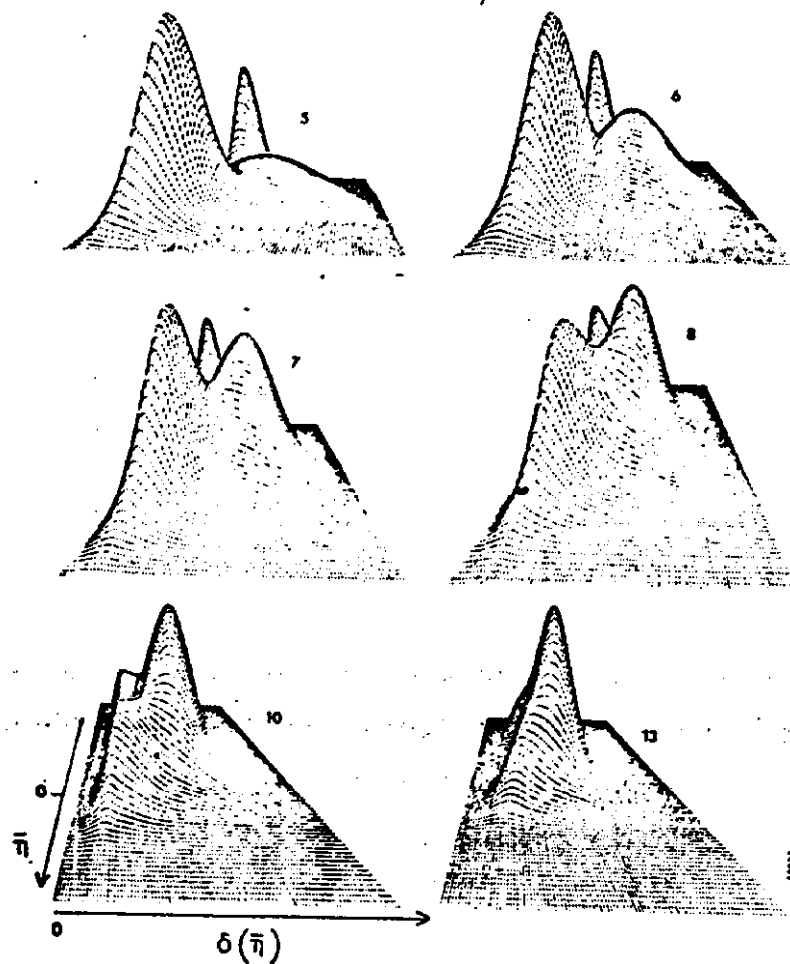


Fig. 5. 3D representation of the number of events as a function of $\bar{\eta}$ and δ for various charged multiplicities at $\sqrt{s} = 63$ GeV (7.1).

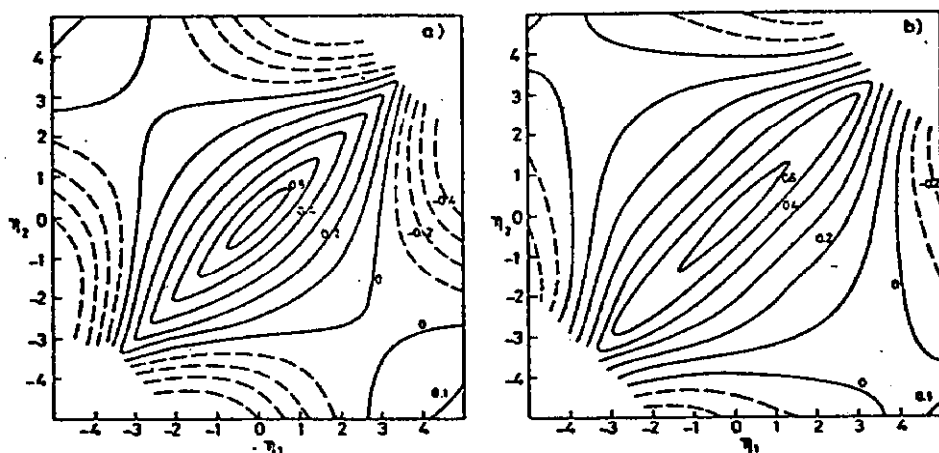


Fig. 5.3. Contours of constant correlation $R(\eta_1, \eta_2)$ in the (η_1, η_2) plane. Contours of negative correlations are shown as dotted lines (74-1). (a) $\sqrt{s} = 23$ GeV; (b) $\sqrt{s} = 63$ GeV.

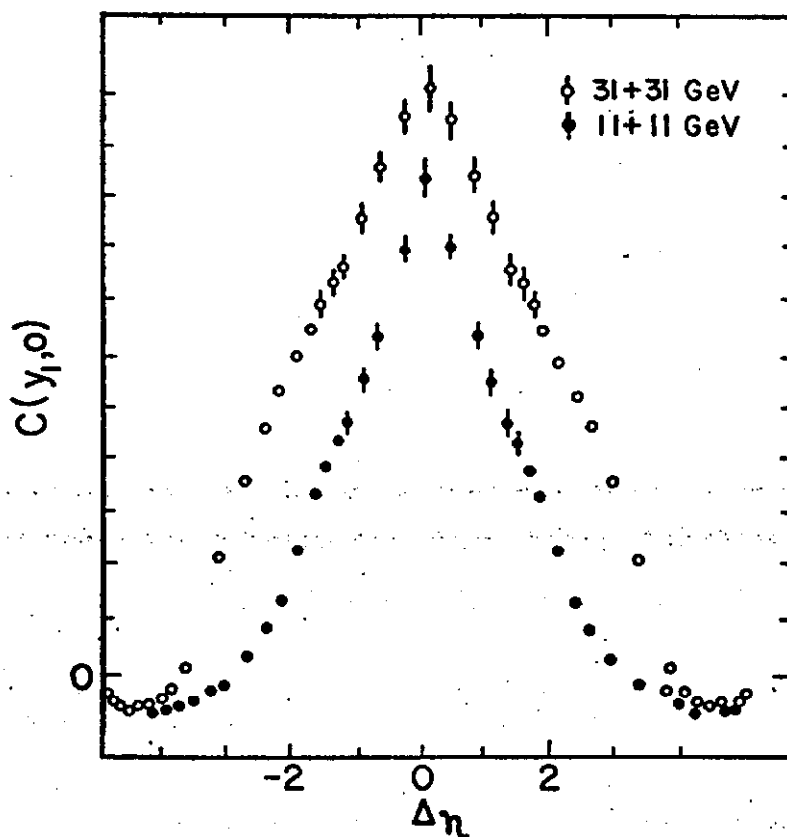


Fig. 5.4. Correlation function $R(\eta_1, \eta_2)$ for fixed η_1 versus η_2 . Full circles refer to $\sqrt{s} = 23$ GeV, open circles to $\sqrt{s} = 63$ GeV (74-1).

$R(\eta_1, \eta_2)$ is on $|\eta_1 - \eta_2|$. Fits of the projections, like those in Fig. 5.4, can be made to dependences of the types:

$$C(\eta_1, \eta_2)_{\eta_1 \text{ fixed}} = A \exp[-|\eta_1 - \eta_2|/L] + \text{Background} \quad (5.10)$$

$$C(\eta_1, \eta_2)_{\eta_1 \text{ fixed}} = A' \exp[-|\eta_1 - \eta_2|^2/4L^2] + \text{Background} \quad (5.11)$$

yielding correlation lengths of $L \simeq 2\ell \simeq 2$, which are short compared to the available rapidity range.

- (iii) The correlation function $R(\eta_1, \eta_2)$ is almost energy independent in the central region, having a maximum of about 0.65. Outside of the central region there is energy dependence. For $\eta_1 = \eta_2$ and large, the s -dependence is basically due to the expansion of phase space as s increases.
- (iv) Along the line $\eta_1 = -\eta_2$ the contours are more separated. At the largest values of $|\eta_1| + |\eta_2|$ there are enhancements, which go to larger $|\eta|$ as s increases. These events are of the diffractive-type and the corresponding particles are emitted in opposite directions.

5.2. Azimuthal Correlations

Other types of correlation functions are defined in the same way as in (5.5) and (5.6). For instance, the correlation function in rapidity and in azimuthal angles may be defined as:

$$R(y_1, \varphi_1, y_2, \varphi_2) = \frac{\sigma_{in} \frac{d^4\sigma}{dy_1 dy_2 d\varphi_1 d\varphi_2}}{\frac{d^2\sigma}{dy_1 d\varphi_1} \frac{d^2\sigma}{dy_2 d\varphi_2}} - 1 \quad (5.12)$$

Since the initial protons are unpolarized $R(y_1, \varphi_1, y_2, \varphi_2)$ is a function only of the difference $\Delta\varphi = \varphi_2 - \varphi_1$. Moreover in the central region the correlation in rapidity depends mostly on the rapidity difference, $\Delta y = y_2 - y_1$. Thus for the central region Eq. (5.12) can be integrated over $\varphi_1 + \varphi_2$ and $y_1 + y_2$, obtaining:

$$R(\Delta y, \Delta\varphi) = \frac{\sigma_{in} \frac{d^2\sigma}{d\Delta y d\Delta\varphi}}{\frac{d\sigma}{d\Delta y} \frac{d\sigma}{d\Delta\varphi}} - 1 \quad (5.13)$$

We shall next discuss the correlations in rapidity and azimuth measured by the Aachen-CERN-Heidelberg-Munich collaboration (ACHM) using a streamer chamber system (74-19, 74-20). Since this experimental equipment is relatively recent, a brief description may be useful.

The I7 intersection region has been surrounded with two double gap streamer chambers, $270 \times 125 \times 50 \text{ cm}^3$ in size; the chambers are placed one above and one below the vacuum chambers and are separated vertically by 8 cm (Fig. 5.5). An inner region with a total volume of $170 \times 70 \times 25 \text{ cm}^3$ was made insensitive because of incompatibility with the bicone structure of the vacuum chamber. A plate made of lead oxide-epoxy separates each chamber volume into an inner region for the detection of charged particles and in an outer region for the detection of conversion electrons from π^0 's. Thus charged tracks are observed over a length of 13 to 30 cm.

The chambers are viewed, via a complex mirror system, by a lens followed by an image intensifier. The system allows to see two 8° stereo views, all views being recorded on a single 35 mm film.

The apparatus is triggered by a coincidence between two scintillation counter hodoscopes, placed around the beam pipes on each side of the intersection region. This trigger, effectively similar to the one used by the Pisa-Stony Brook collaboration, allows the observation of about 90% of the inelastic cross section. The pictures were scanned and selected events were measured with conventional image plane digitizers.

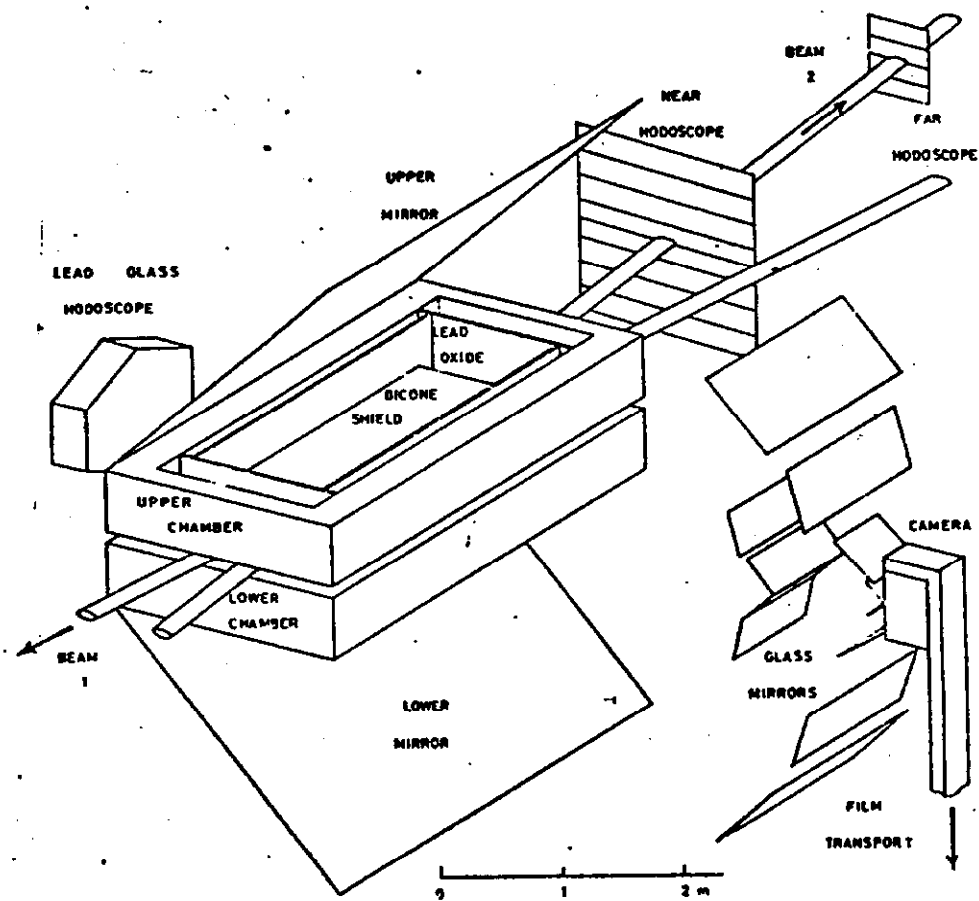


Fig. 5.5. Layout of the streamer chamber set up in I7 (74-20).

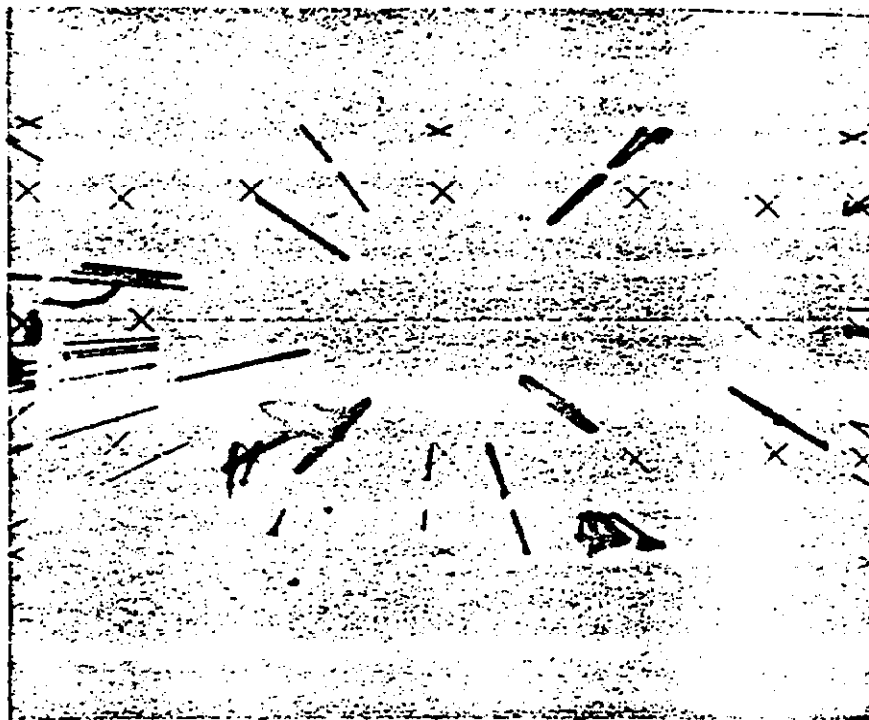


Fig. 5.6. Picture of an event in the streamer chamber set up (74-20).

The experimental results which will be discussed concern the correlations among charge tracks only. As in the Pisa-Stony Brook experiment, only angles are measured. The two experiments are quite similar. For each track one has θ and ϕ in the c.m. system and the pseudorapidity is again computed using formula (5.7). The two experiments yielded results in good agreement with one another.

An event observed with the streamer-chamber system is shown in Fig. 5.6.

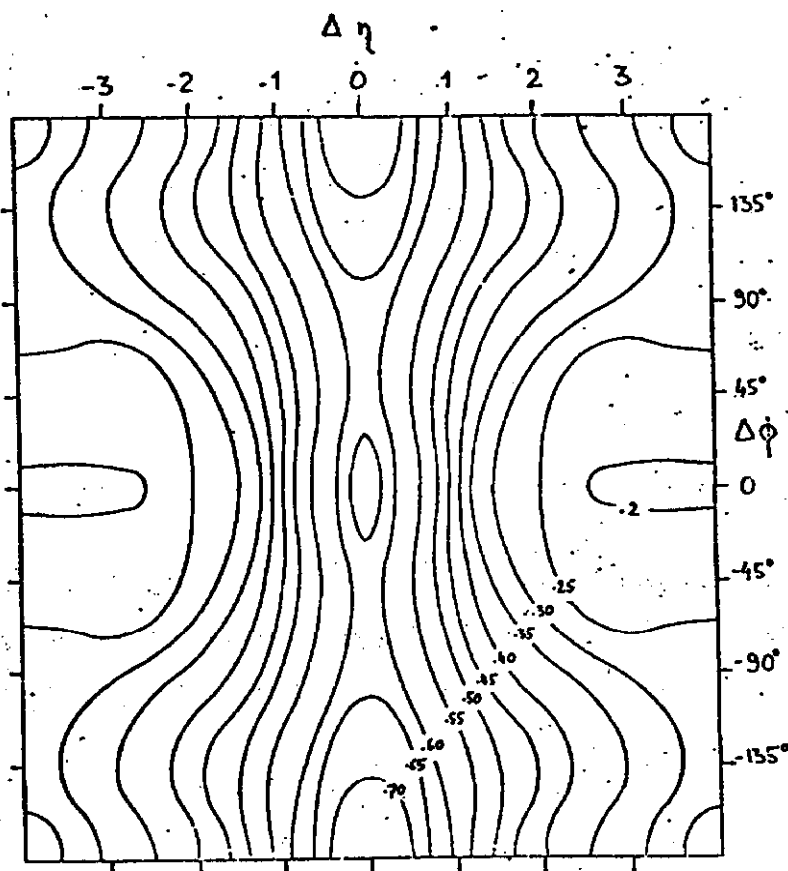


Fig. 5.7. Contours of constant correlation $R(\Delta\eta, \Delta\phi)$ in the $(\Delta\eta, \Delta\phi)$ plane (74-20).

The contours of the two-particle correlation function $R(\Delta\eta, \Delta\varphi)$ at $\sqrt{s} = 52.7$ GeV are shown in Fig. 5.7 as a function of $\Delta\eta = \eta_2 - \eta_1$ and $\Delta\varphi = \varphi_2 - \varphi_1$ for values of $|\eta_1 + \eta_2| < 3$. For fixed $\Delta\varphi$ (in particular $\Delta\varphi = 0$) one finds again the rapidity correlations already discussed. The graph shows that there are weak correlations in φ , which depend on $\Delta\eta$. In particular the larger the rapidity difference $\Delta\eta$ between the two particles, the more probable it is to find the two particles at large $\Delta\varphi$, that is to find them going in opposite directions.

The authors try to explain the features of Fig. 5.7 in the framework of the independent cluster model of particle production. In this model the $\Delta\varphi$ dependence of $R(\Delta\eta, \Delta\varphi)$ reflects correlations within the same cluster. Instead the $\Delta\eta$ dependence of $R(\Delta\eta, \Delta\varphi)$ can be used to obtain estimates of the parameters describing the decomposition into clusters.

The large $\Delta\varphi$ correlation at large $\Delta\eta$ can be qualitatively interpreted in the independent cluster model as an effect of energy-momentum conservation within one cluster. From the dependence of R on $\Delta\eta$ the authors estimate that the average number of particles per cluster is 1.9. These results cannot be considered a proof of the validity of the cluster model, but only of its usefulness as a method of parametrization.

5.3. Transverse Momentum Correlations

The experimental results on p_t correlations obtained by the Saclay group (74-10) will now be discussed. The group used two magnetic spectrometers facing each other and at 90° to the beams in the 11 intersection region (see Fig. 5.1). The angular region covered by each spectrometer was relatively small ($\Delta\Omega_1 \simeq 0.062$ sr, $\Delta\Omega_2 = 0.22$ sr) so that one can consider with good approximation that $y_1 = y_2 = 0$, $\Delta\varphi = \varphi_2 - \varphi_1 = 180^\circ$. Particle trajectories were reconstructed from magnetostrictive wire spark chambers; particle identification was done with time of flight.

The apparatus allowed the direct measurement of the double differential cross section for a double inclusive cross section with complete particle identification up to 1 GeV/c.

Figure 5.8 shows the double differential invariant cross section

$$f(p_1, p_2) = \frac{d^6\sigma}{d^3p_1 d^3p_2 \frac{E_1}{E_2}} \quad (5.14)$$

for $\pi^+\pi^-$ inclusive production plotted versus $p_{t\pi^+}$ for four values of $p_{t\pi^-}$. Very similar graphs exist also for the inclusive production of $\pi^-\pi^-$ and $\pi^+\pi^+$ pairs. The distributions fitted to exponential functions of the form

$$f(p_1, p_2) = Ae^{-Bp_{t\pi^+}} \quad (5.15)$$

yield values of the slopes B very close to the values found in single pion production, with only a minor dependence on $p_{t\pi^-}$. These effects are better illustrated in Fig. 5.9, which shows the average of p_{t2} , $\langle p_{t2} \rangle_{p_{t1}}$, computed for various constant values of p_{t1} .

The p_t -correlation functions

$$R(p_{t1}, p_{t2}) = \frac{\sigma_{in} \frac{d^2\sigma}{dp_{t1} dp_{t2}}}{\frac{d\sigma}{dp_{t1}} \frac{d\sigma}{dp_{t2}}} - 1 \quad (5.16)$$

for $\pi^+\pi^-$, $\pi^+\pi^+$ and $\pi^-\pi^-$ pairs are shown in Fig. 5.10 plotted versus

$|p_{t1}| + |p_{t2}|$ at $\sqrt{s} = 52$ GeV. $R_{\pi^+\pi^-}$ is always somewhat larger than $R_{\pi^+\pi^+}$ and $R_{\pi^-\pi^-}$ which are almost equal. In particular $R_{\pi^+\pi^-}$ is largest at small values of the transverse momentum and one may loosely speak of an "attraction" between low energy π^+ and π^- .

The authors considered also integrated correlations

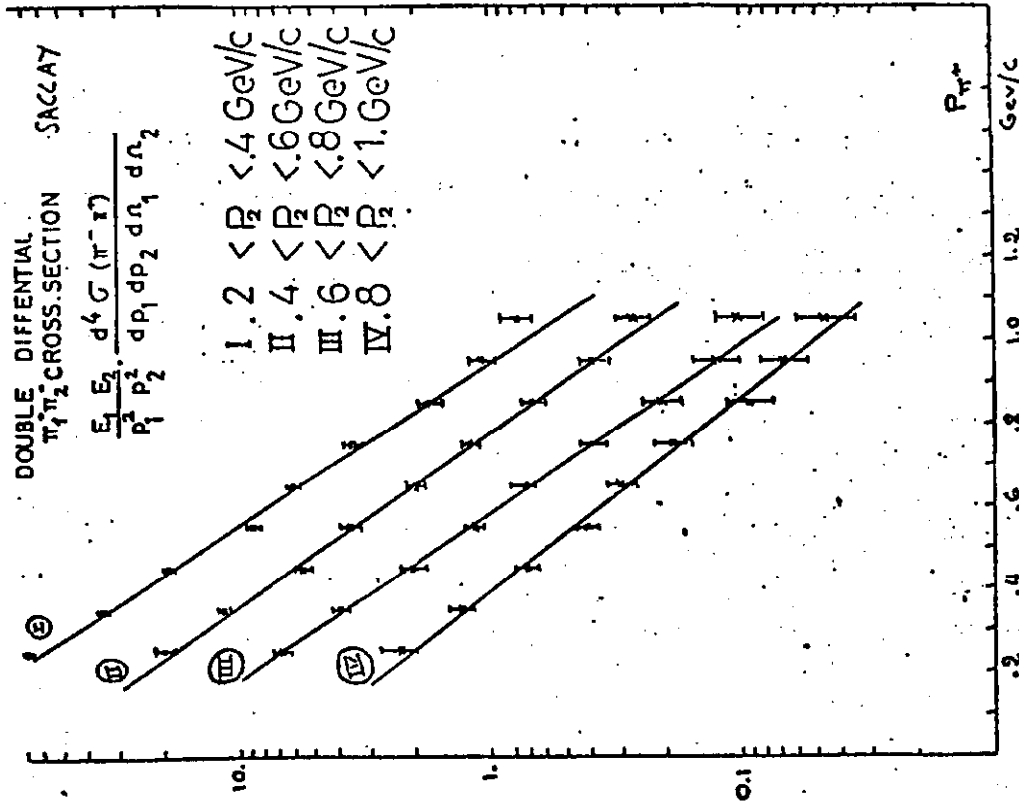


Fig. 5.8. Double differential cross sections for $\pi^+ \pi^-$ pairs as a function of $p_{t\pi^-}$ for four different values of $p_{t\pi^+}$ (74-24).

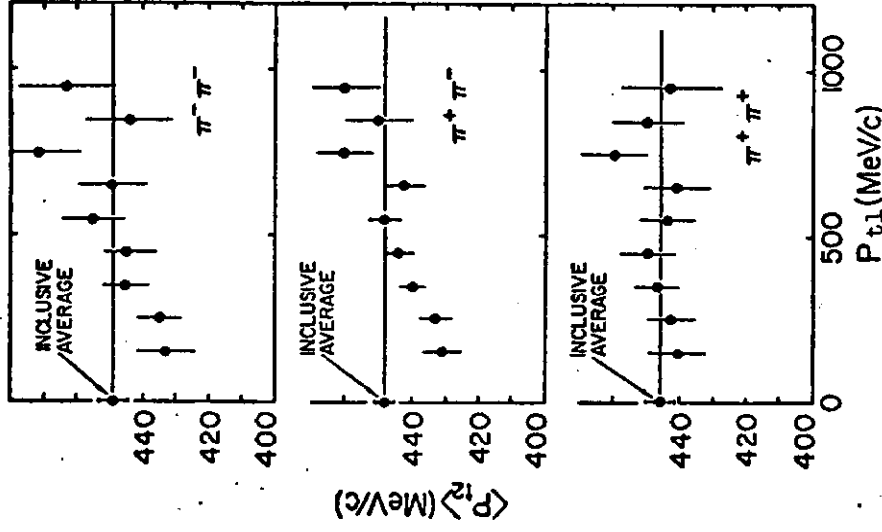


Fig. 5.9. The average value of p_{t2} as a function of p_{t1} for $\pi^+ \pi^-$, $\pi^+ \pi^+$ $\pi^- \pi^-$ pairs (74-24).

$$C_{12} = \frac{\sigma_{in} \int d\sigma_{12}}{\int d\sigma_1 \int d\sigma_2} \quad (5.17)$$

and found

$$C_{\pi^+ \pi^-} \simeq 1.64 > C_{\pi^+ \pi^+} \simeq C_{\pi^- \pi^-} \simeq 1.3 \quad (5.18)$$

$$C_{pp} \simeq C_{\bar{p}\bar{p}} \simeq 2C_{\pi^+ \pi^-}, \quad (5.19)$$

that is the correlation between pions of opposite sign is larger than the correlations between pions of the same sign. Moreover the correlation between two protons and between $p\bar{p}$ pairs is about equal and twice as large as the correlation between $\pi^+ \pi^-$ pairs.

One concludes that transverse momentum correlations exist and are more important at small p_t .

5.4. Rapidity Correlations with a Fast Forward Particle

As an example of a special correlation on rapidity we shall discuss the experiment of the CERN-Pisa-Rome-SUNY collaboration (74-9). (See Fig. 5.1.) The Pisa-Stony Brook 4π -hodoscope counter system was placed in coincidence with the CERN-Rome small angle magnetic spectrometer, which accepts negative particles emitted at essentially 0° in the c.m. system ($p_t \simeq 0$) and with $0.4 < x < 0.8$, $|y_{lab}| < 0.9$ (74-9). Thus the forward negative particle, which is identified by means of threshold gas Cerenkov counters, is already in the fragmentation region. The collaboration studied the rapidity correlation between the forward negative particle and charged tracks in the almost inclusive reaction

$$pp \rightarrow \begin{pmatrix} \pi^- \\ K^- \\ \bar{p} \end{pmatrix} + (n \text{ charged tracks}) \quad (5.20)$$

The following rapidity correlation function was considered:

$$R(y, \eta) = \frac{\sigma_{\text{in}} \frac{d^2 \sigma}{dy d\eta}}{\frac{d\sigma}{dy} \frac{d\sigma}{d\eta}} - 1 \approx \frac{\Delta N(\eta) M_0}{\Delta N_0(\eta) M} - 1 \quad (5.21)$$

where y is the rapidity of the forward negative particle and η is the pseudorapidity of the charged tracks, M_0 is the total number of inelastic triggers in which at least one charged particle was produced in each of the forward and backward hemispheres of the Pisa-Stony Brook counter system. M is the total number of triggers in which one had also a negative particle in the forward spectrometer. $\Delta N_0(\eta)$ and $\Delta N(\eta)$ are the corresponding numbers of events in an interval $\Delta\eta$ at η .

Figure 5.11 gives $R(y_{\pi^-} = 5, \eta)$, $R(y_{K^-} = 3.8, \eta)$ and $R(y_{\bar{p}} = 3.1, \eta)$ at $\sqrt{s} = 53$ GeV ($x_{\text{negative}} = 0.4$ for π^- , K^- , \bar{p}). One notices that:

- (i) the correlation function for the three particles is similar;
- (ii) the correlation is largest and positive for particles with large negative values of η (these particles are emitted in the backward hemisphere with respect to the forward going fast negative particle); it decreases with increasing η and has a peak at large positive values of η ;
- (iii) the correlation functions have at most a weak energy dependence;
- (iv) the forward peak in the correlation function is associated with low multiplicity events and is already located at a pseudorapidity value such that $y - \eta \approx 1.3$.

Undoubtedly conservation of momentum and of charge explains most of the qualitative features of $R(\eta)$. In fact the trigger, which selected interactions containing a high-momentum, negative particle going in the direction of one of the incident protons, provides a sample of nontypical pp interactions.

A plausible explanation of the peak in the correlation function is in terms of a process of the type:

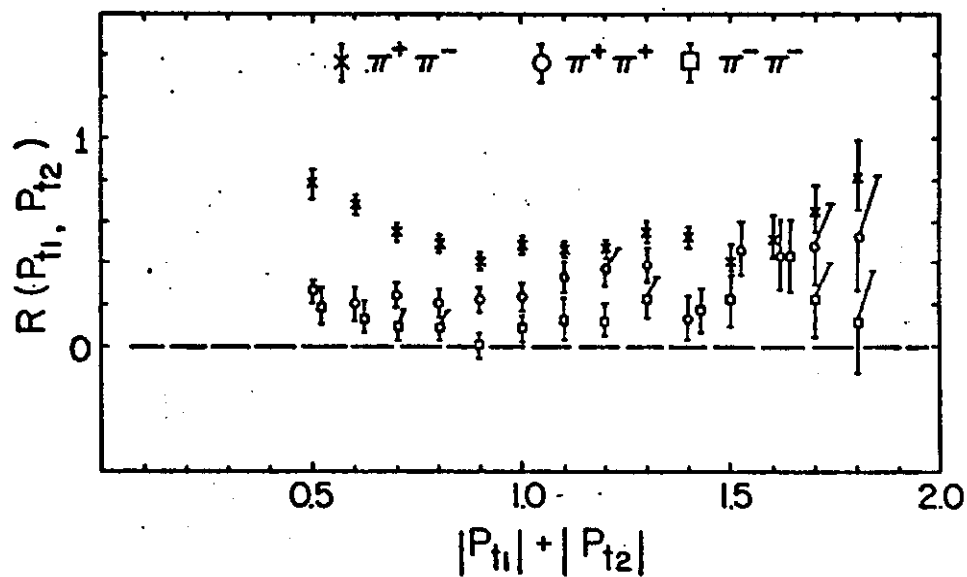


Fig. 5.10. The p_t correlation function (5.16) plotted versus $|p_{t1}| + |p_{t2}|$ for $\pi^+\pi^-$, $\pi^+\pi^+$ and $\pi^-\pi^-$ pairs at $\sqrt{s} = 53.7$ GeV (74-24).
 $\sqrt{s} = 53$ GeV

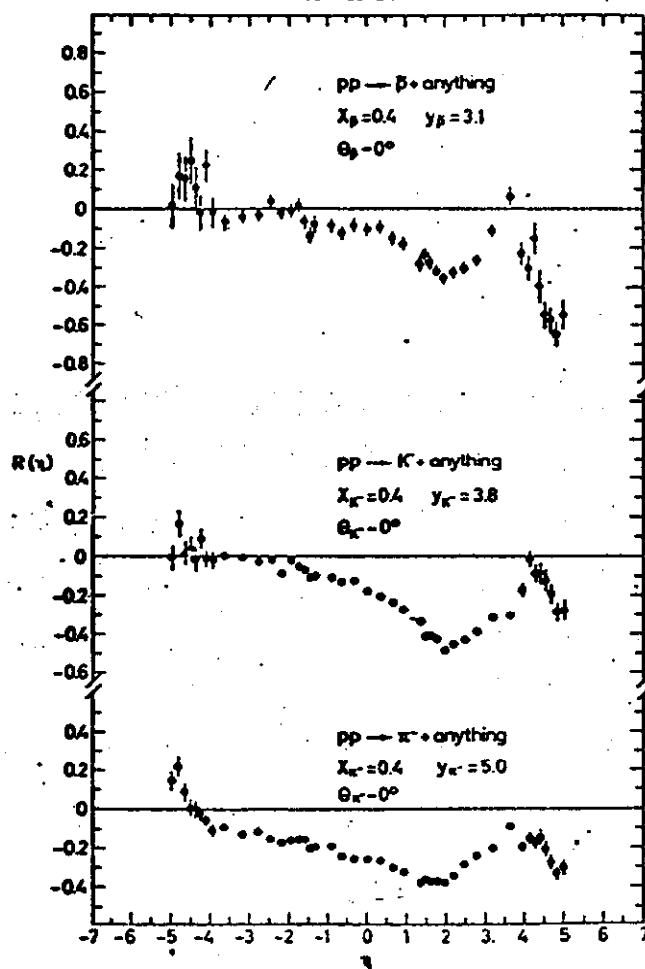


Fig. 5.11. The correlation function $R(y, \eta)$ of Eq. (5.21) for π^- , K^- and \bar{p} of $x = 0.4$ at $\sqrt{s} = 53$ GeV (74-9).

$$pp \rightarrow p + C^+ \quad (5.22)$$

$$\quad \quad \quad \searrow \rightarrow p\pi^+\pi^-, K^-, \bar{p}$$

where C^+ indicates a cluster of particles, whose nature is open to discussion, which gives rise to a low multiplicity event, with particles going in the same hemisphere. A Monte Carlo calculation gave $m_C \simeq 2$ GeV for the π^- case, 2.2 GeV for K^- and 3.1 for the \bar{p} . C^+ would decay into 3-4 particles. This experiment suggests that besides pions, also kaons and antiprotons could be produced via a cluster of particles.

Similar types of correlations were performed also by the CHLM group, which added a system of scintillation counters around $\theta_{cm} \sim 90^\circ$, to their small angle spectrometer (74-17). Thus they could study the correlations between a fast forward π^+ , p or \bar{p} and a second charge particle in the central region. The results show both short range and long range correlations for each type of identified particles. Interpreting the results in terms of a cluster model they conclude that (i) for every cluster with a \bar{p} , there are about 20 with a p ; (ii) 50% of the clusters emitted at $y \simeq 2.4$ contains a proton; (iii) a cluster decays into 3-4 particles.

6. DIFFRACTIVE PROCESSES. EXCLUSIVE REACTIONS

Under the general term of diffractive processes we shall classify a number of reactions characterized by: (i) low momentum transfers, (ii) no quantum numbers exchanged and (iii) essentially no energy dependence. In practice these features concern:

- (i) the inclusive production of protons at values of x close to 1 (leading particle effects);
- (ii) reactions of the type $pp \rightarrow pN^*$, $\rightarrow N^*N^*$ (single and double diffraction dissociation). This class of reactions may contain also reactions where the N^* is not a well defined state. The N^* states extend to relatively large masses, larger than 10 GeV.

- (iii) Exclusive reactions with a relatively large cross sections. In fact these reactions may be observed at the ISR, only if they proceed via diffractive processes, that is processes in which the energy dependence is small.

The diffractive cross section is large. In fact the total cross section may be split as follows:

$$\sigma_{\text{tot}} = \sigma_{\text{el}} + \sigma_{\text{in}} \quad (6.1)$$

$$\sigma_{\text{in}} = \sigma_{\text{SD}} + \sigma_{\text{DD}} + \sigma_{\text{ND}} \quad (6.2)$$

where $\sigma_{\text{SD}} = \sigma_{\text{AD}} + \sigma_{\text{BD}}$ is the single diffraction dissociation cross section and is equal to the sum of the diffraction dissociation cross sections of A and B (which are equal in the case of pp collisions); σ_{DD} is the double diffraction dissociation and σ_{ND} is the inelastic non-diffractive cross section. At the ISR at $\sqrt{s} = 55$ GeV one has, approximately:

$$\sigma_{\text{tot}} \simeq 43 \text{ mb}$$

$$\sigma_{\text{el}} \simeq 6-7 \text{ mb} \simeq \sigma_{\text{SD}} = \sigma_{\text{AD}} + \sigma_{\text{BD}} \quad (6.3)$$

$$\frac{\sigma_{\text{DD}}}{\sigma_{\text{el}}} \simeq \frac{1}{4} \left(\frac{\sigma_{\text{SD}}}{\sigma_{\text{el}}} \right)^2 \sim 1.6 \text{ mb}$$

6.1. Leading Particle Effects

Figure 6.1 shows the invariant cross section for the inclusive production of protons in the kinematical region of x close to 1, as measured by the small angle spectrometer of the CHLM collaboration in I2 (73-16). The distribution has a peak at $x \simeq 0.99$, which seems to be energy independent. The shape of the distribution at smaller values of x reflects the spectrum of masses produced in the opposite hemisphere. The peak may be interpreted as

due to the single diffraction excitation of one nucleon, which breaks up into a mass $M^2 \simeq s(1-x)$, while the observed proton remains intact.

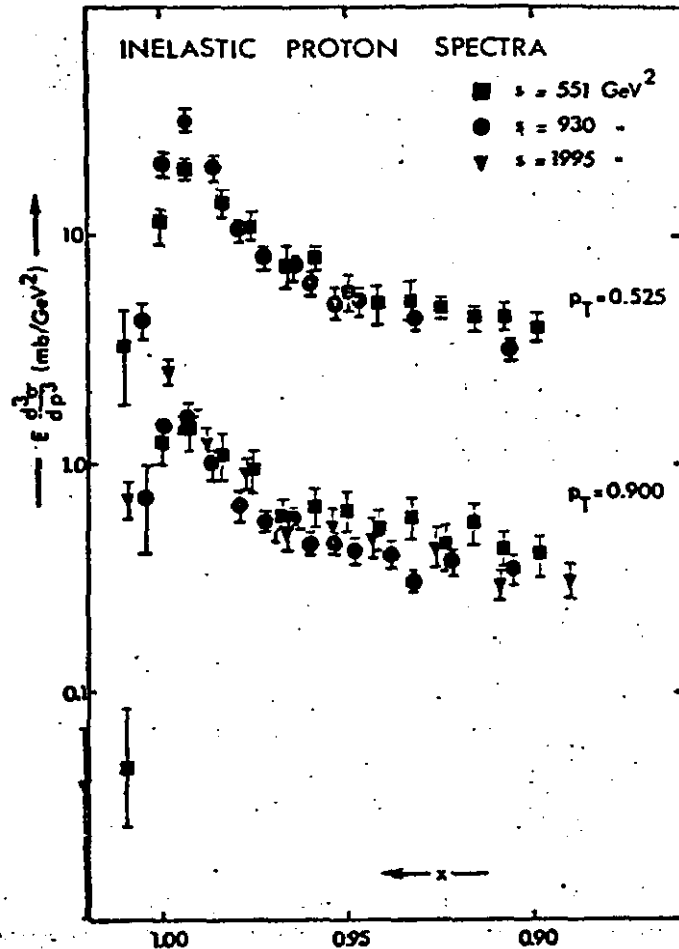


Fig. 6.1. Inelastic proton spectra at various ISR energies and fixed p_T , at high x (73-16).

Both the peak at $x \sim 0.99$ and the broad structure at $x \sim 0.5$ (see Fig. 4.4) have been interpreted within the framework of the triple-Regge-exchange picture.

The energy independence of the cross section and the shape of the missing mass distribution suggested that the $x \sim 0.99$ bump could be interpreted as due to triple Pomeron exchange only, (PPP), and could be described with the equation

$$f = E \frac{d^3\sigma}{d^3p} \approx \frac{G_{PPP}(t)}{16\pi^2} \left(\frac{M^2}{s} \right)^{1-2\alpha_P(t)} \quad (6.4)$$

The data are consistent with an effective Pomeron trajectory of

$$\alpha_P(t) = 1.0 + 0.2t \quad (6.5)$$

The broad structure at medium x was instead interpreted as arising from a PRR exchange, where R is an effective meson trajectory. This yields the equation

$$f \approx \frac{G_{PRR}(t)}{16\pi^2} \left(\frac{M^2}{s} \right)^{1-2\alpha_R(t)} \quad (6.6)$$

and the ISR data are consistent with an effective meson trajectory.

$$\alpha_R = 0.45 + 0.75t \quad (6.7)$$

with $G_{PRR}(t) \approx 1100 \text{ mb/GeV}^2$, independent of t .

6.2. Correlations for Diffractive Events

Qualitative informations on the main features of diffractive events have been obtained by the Pisa-Stony Brook, CHLM and ACHGT collaborations studying different types of correlations. We have already mentioned some results of the Pisa-Stony Brook work on correlations (see Figs. 5.2 and 5.3), in particular the result that diffractive events have a relatively low multiplicity.

As already discussed in Section 5.4, the CHLM collaboration measured rapidity correlations between a high energy proton in their small-angle spectrometer and charged particles going in the opposite hemisphere or at 90° .

Figure 6.2 shows their data in terms of the rapidity of the proton measured in the spectrometer and of the pseudorapidity of the charged particles in the

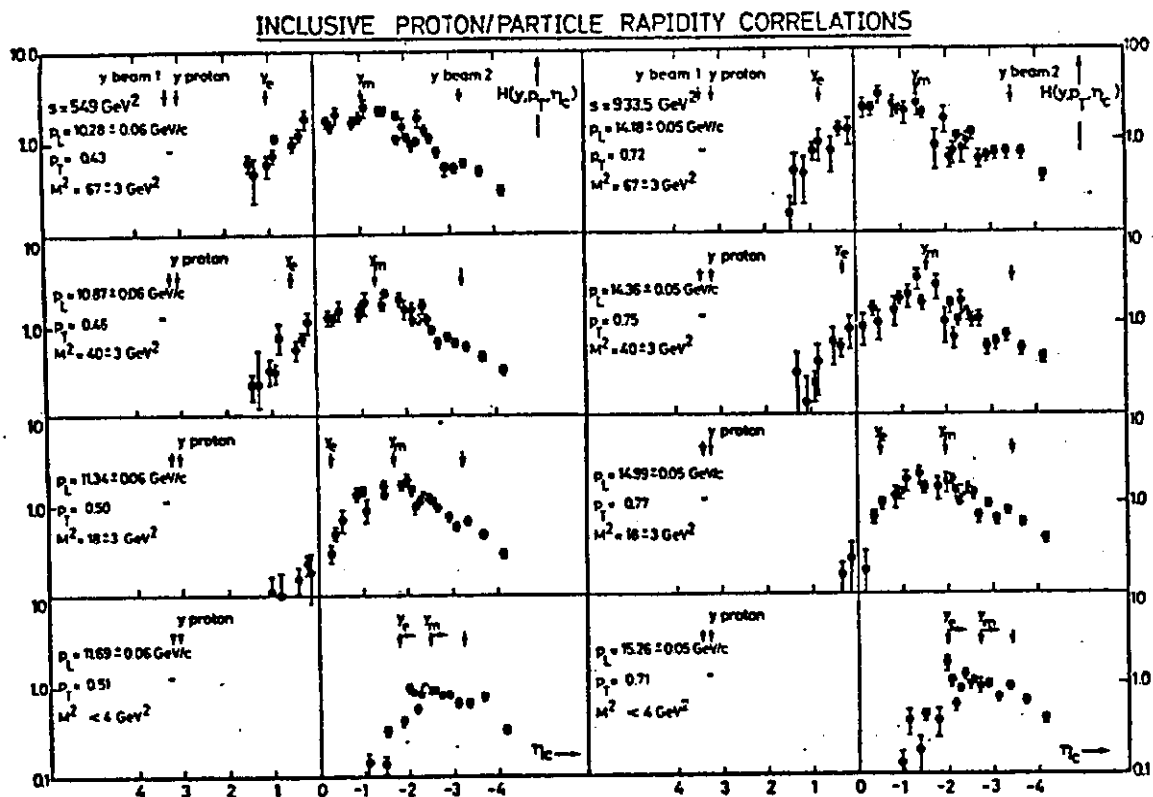


Fig. 6.2. Rapidity correlations between a fast forward proton and a charged particle as function of their relative rapidity (pseudorapidity) plotted for different values of p_L , p_T , M^2 (74-25). The arrows mark the rapidities of beam 1, beam 2, the identified proton, the center and half values of the distributions.

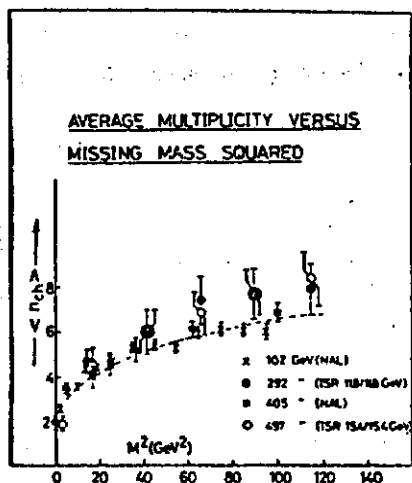


Fig. 6.3. Average charged particle multiplicity of the X system in $pp \rightarrow p + X$ plotted versus the mass squared of X (74-25).

counters. The data show a gradual increase of the rapidity gap as the momentum of the proton detected in the spectrometer is raised from $x = 0.9$ (where fragmentation protons probably make up the bulk of the cross section) to $x = 0.99$ (where diffracted protons dominate the cross section). By integrating the graphs of Fig. 6.2, the group obtained the mean charged multiplicity in the scintillation counters. This is plotted in Fig. 6.3 versus the missing mass squared, M^2 . The multiplicity increases with M^2 , and seems to level off at large M^2 .

The set up of the ACHGT collaboration, used to measure elastic scattering, was also used to detect quasi elastic scattering (74-31). The experimental layout, consisting of two magnetic spectrometers placed along the two beams, in opposite directions was triggered by a coincidence between charged particles, one in each spectrometer (Fig. 5.1). After removing elastic scatterings, the remaining events were qualitatively classified according to the number of charged particles observed in counter hodoscopes surrounding the apertures of each of the two spectrometers:

- (i) Low multiplicity events, for which no extra tracks were recorded.

Figure 6.4c shows a bi-dimensional plot of these events; the horizontal scale gives charge (positive or negative) and x-value of particle 1, while the vertical scale gives the same quantities for particle 2. The events cluster along two lines, one for $x_1 \sim 1$ and the other for $x_2 \sim 1$. These events correspond to single diffraction, that is to reactions of the type $pp \rightarrow pN^*$.

- (ii) The diffraction bands are still observed in the case of one particle on one side and many particles on the opposite side. One still observes single diffraction.
- (iii) In the case of "two jets" of particles going in opposite directions one does not observe anymore the clustering at $x_1 \sim 1$ or $x_2 \sim 1$.

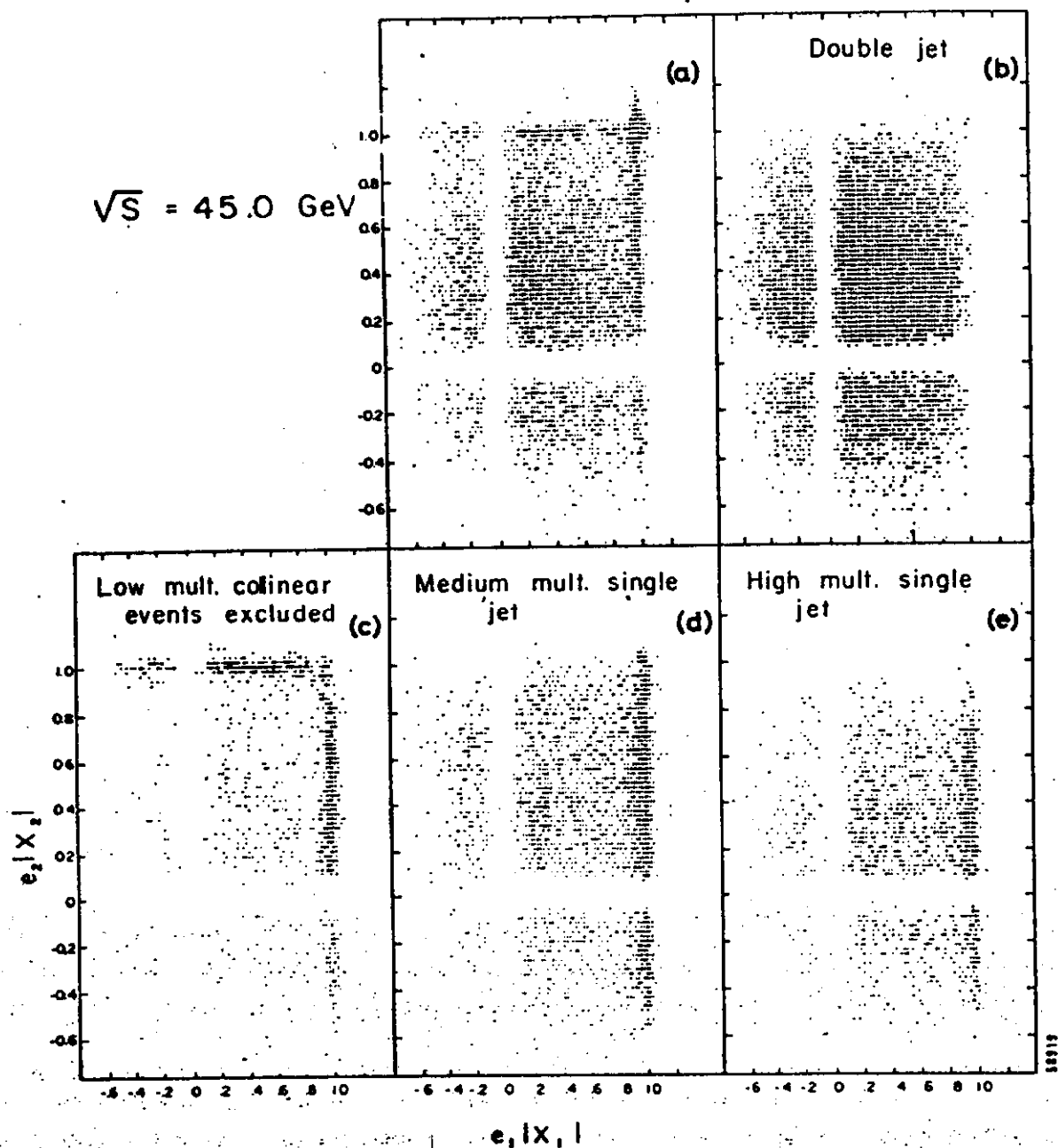


Fig. 6.4. Plot of $e_2|x_2|$ versus $e_1|x_1|$ at $\sqrt{s} = 45 \text{ GeV}$; x_1 and e_1 are the Feynman variable and the charge of the particle 1 in spectrometer 1, respectively. (a) Sample of the entire data; (b) to (e) the distributions for various multiplicity cuts. In (d) and (e) the subscript 2 indicates the arm containing the jet (74-31).

Figure 6.5 shows the missing mass distribution for the same events, plotted for different multiplicities.

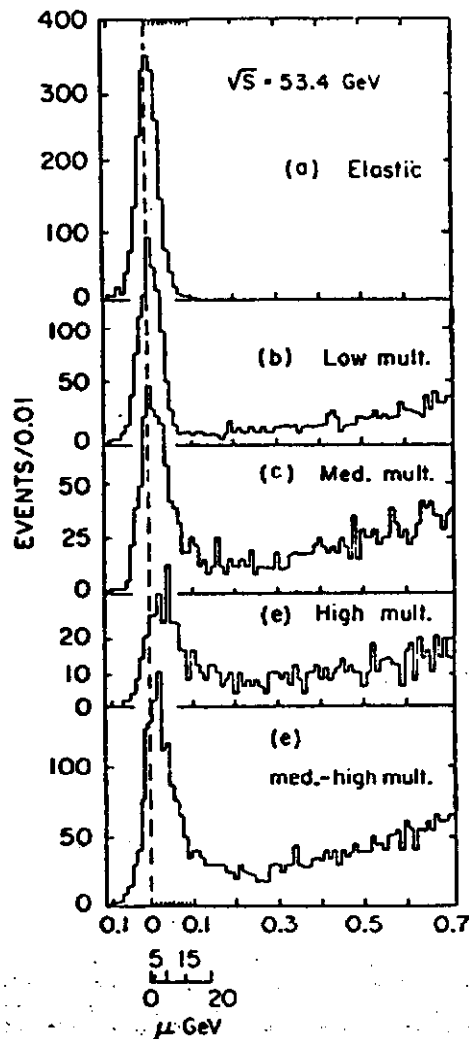
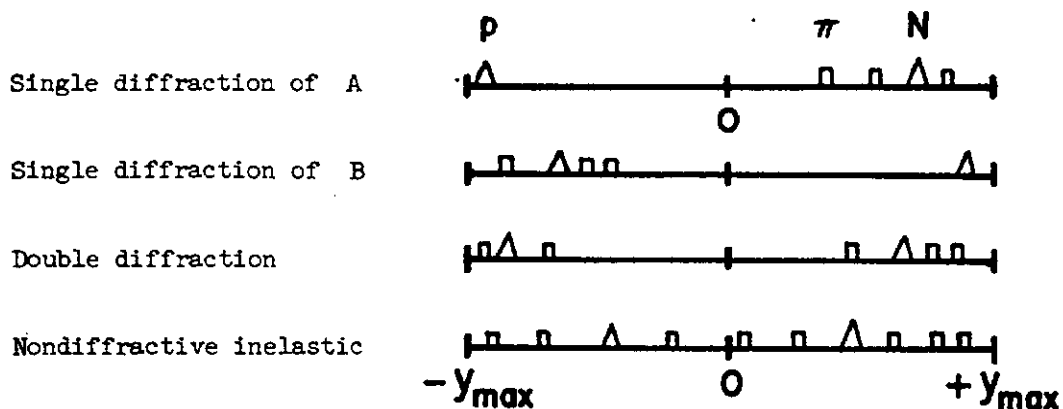


Fig. 6.5. Distribution in M^2/s , where M is the missing mass for elastic and single-jet events, at $\sqrt{s} = 53 \text{ GeV}$ (74-31).

From the above results emerges a clear picture of diffraction processes: one finds both single and double diffraction processes of the type $pp \rightarrow p + N^*$; $N^* + N^*$. These events exhibit the following qualitative distribution in rapidities:



The nature of the N^* needs further analysis, in particular in exclusive reactions.

6.3. Exclusive reactions

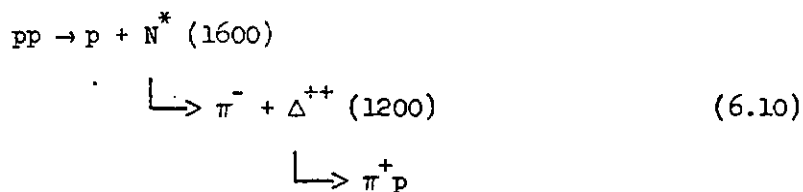
6.3.1. The reaction $pp \rightarrow (p\pi^+\pi^-)p$

The two-arm spectrometer of the ACGHT collaboration was modified by the ACHLR (private communication) and ACL (74-26) collaborations, by placing the two septum magnets one above the other, on the same side from the interaction region, as sketched in Fig. 5.1. The fast trigger required three identified charged particles in the two magnets and 1 particle in the proportional chambers on the other side. A system of anticounters surrounded the intersection region at 90° to the beams. The groups were thus able to select events of the reactions:

$$pp \rightarrow (p\pi^+\pi^-) + p \quad (6.8)$$

$$\rightarrow (p\pi^+\pi^-) + X \quad (6.9)$$

with $x_{(p\pi^+\pi^-)} \simeq 1$. A detailed analysis of the effective mass distributions shows that reaction (6.8) proceeds in part via the chain:



The reaction (6.9) is interpreted as a double diffraction dissociation reaction.

The ratios of the cross sections

$$R_1 = \frac{\sigma(pp \rightarrow pX)}{\sigma(pp \rightarrow pp)} \tag{6.11}$$

$$R_2 = \frac{\sigma(pp \rightarrow p\pi^+\pi^-X)}{\sigma(pp \rightarrow p\pi^+\pi^-p)} \tag{6.12}$$

as functions of t are approximately:

$t(\text{GeV}/c)^2$	0.21	0.33	.46
R_1	2%	6%	18%
R_2	3%	9%	14%

One has $R_1 \simeq R_2$ and one has evidence for the approximate validity of factorization.

The slopes b of the exponential t -distributions are approximately $b \sim 10$ for elastic scattering, $b \sim 6$ for the single diffraction dissociation reaction (6.8) and $b \sim 4$ for the double dissociation reaction (6.9).

Within errors there seem to be no energy dependence of the cross sections in the ISR range, thus confirming the diffractive nature of these reactions.

6.3.2. The reaction $pp \rightarrow p(n\pi^+)$

Preliminary results on the reaction

$$pp \rightarrow p(n\pi^+) \tag{6.13}$$

at small t -values and at $\sqrt{s} = 53$ GeV were reported at the London Conference by the CHOV collaboration (74-14). They used the split Field Magnet facility in the configuration illustration Fig. 3.3 and sketched in Fig. 5.1. The fast trigger required a neutron together with two charged tracks in opposite directions. The slow trigger then selected events with two and only two charged tracks plus the neutron.

Figure 6.6 shows the $n\pi^+$ effective mass distribution for the cases in which the neutron goes in the same general direction of the π^+ ($\cos \theta_J < 0$) and when it goes in the opposite direction ($\cos \theta_J > 0$). In the first case the $n\pi^+$ mass distribution exhibits a number of peaks corresponding to N^* resonances; that is the reaction (6.13) proceeds sometime via the chain



For $\cos \theta_J > 0$ the resonance signal is much weaker. The t -dependence for the cross sections of reactions of the type (6.14) is shown in Fig. 6.7 for different N^* mass regions. The distributions exhibit a change in slope at $|t| \simeq 0.3$ (GeV/c)². The data for $|t| < 0.2$ (GeV/c)² (< 0.4 for the higher N^* masses) were fitted to exponential functions. From the fits and from inspection of Fig. 6.7 one concludes:

- (i) The slope of the t -distribution is rapidly decreasing with increasing N^* mass; this confirms the results discussed in the previous paragraph.
- (ii) At fixed N^* mass, the slope increases with s , at approximately the same rate as in elastic scattering. Thus shrinking seems to be a phenomenon shared by elastic and inelastic diffraction scattering.

The integration of the angular distribution yields a cross section which decreases as $s^{-0.4 \pm 0.1}$ when s goes from $s = 50$ to $s = 3000$ GeV².

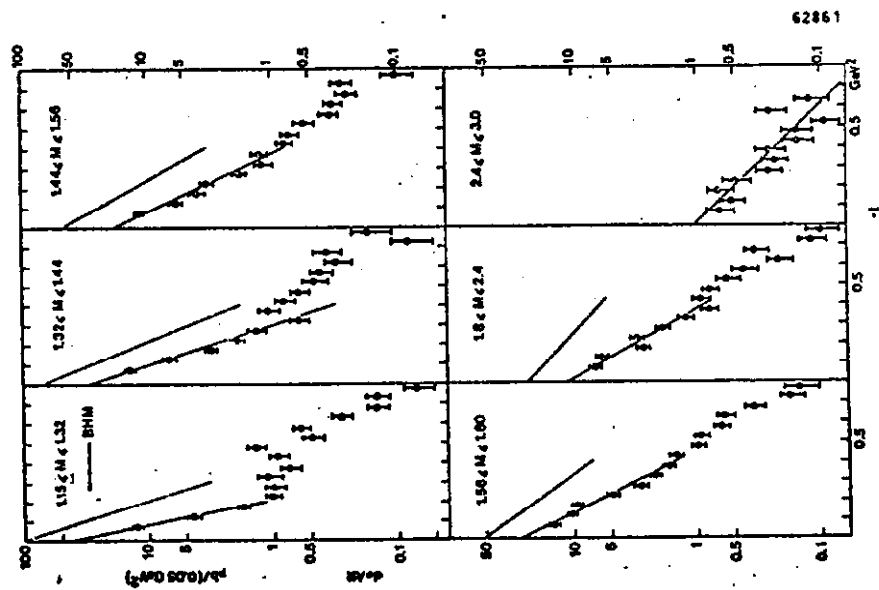


Fig. 6.7. t -dependence of $d\sigma/dt$ dM ($pp \rightarrow pn\pi^+$) for various mass regions. Solid lines are exponential fits to the small t -regions; dashed lines are fits to the 24 GeV/c data (74-14).

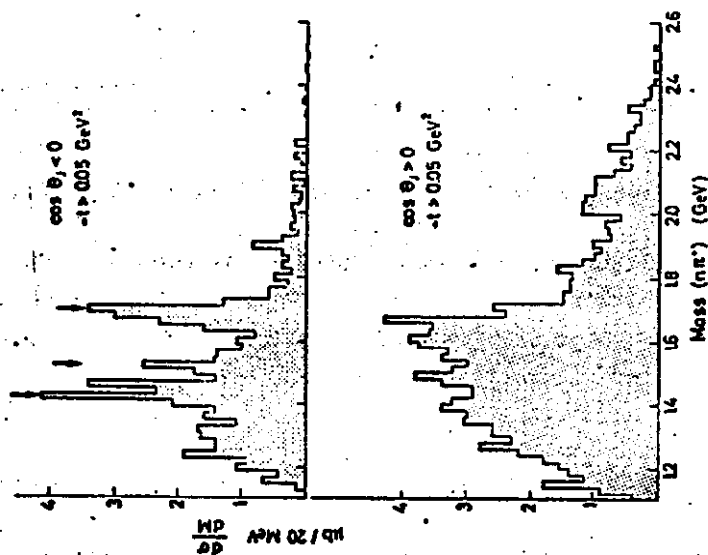


Fig. 6.6. $(n\pi^+)$ effective mass spectra in the reaction $pp \rightarrow pn\pi^+$ at $\sqrt{s} = 53$ GeV and $|t| < 0.05$ (GeV/c) 2 for (a) backward neutrons ($\cos \theta_j < 0$) and (b) forward ones ($\cos \theta_j > 0$) (74-14).

7. PROCESSES AT LARGE p_t

Processes involving the production of particles at large transverse momenta have been reviewed at this symposium by J. Cronin. In the following we shall only summarize some of the main features observed at the ISR.

Large p_t -phenomena have always been associated with small distances and experiments on large p_t -phenomena are supposed to probe the inner substructure of the nucleon. In this picture the exponential fall off in p_t for $p_t < 1 \text{ GeV}/c$ corresponds to the extended structure of the proton acting globally as a coherent source. Instead the p_t -dependence at larger transverse momenta would arise from more localized sources inside the proton. Measurements performed until now have shown that the x -dependence and the s -dependence of the invariant cross sections for the inclusive production of large p_t events are smooth functions, which join smoothly to the cross sections at smaller transverse momenta. Thus no new phenomena (or new spatial regions) are easily revealed by inspection of the graphs. Further interpretations require the use of specific models. At present one may interpret the data in terms of constituents models (like parton-parton scattering), but this interpretation is not compulsory. Other, more conventional models, which for instance interpret the large p_t events as arising from the decay of heavy objects, like fireballs, are still tenable. It is hoped that correlation experiments may shed new light on these phenomena, but one has to be careful to properly interpret the kinematics effects.

Table 7.1 gives a list and some of the parameters of the experiments on large p_t -phenomena presented at the 1974 London Conference by groups working at the ISR.

Figure 5.1b gives a sketch of the correlation experiments listed in Table 7.1.

TABLE 7.1

ISR Experiments on Large P_t Phenomena Presented at the 1974 London Conference
(from Landshoff)

Collaboration	Trigger particle			θ_{CM}	Data	Reference
		Max P_T				
Aachen- CERN- Heidelberg- Munich	$^0\pi$	3		90°, 60°	Associated charged-particle multiplicities and correlations	74-19
British- Scandinavian	$^{\pm}\pi, K^{\pm}, p, \bar{p}$	5		40 - 90°	Single-particle distributions	74-8
CERN- Columbia- Rockefeller	$^0\pi$	9		60 - 90°	Single-particle distribution. Associated charged-particle multiplicities and correlations	74-22
CERN- Columbia- Rockefeller- Saclay	γ	4		90°	Momenta of associated charged particles	74-11
CERN- Daresbury- Rutherford- Liverpool	$^{\pm}h$	3.5		90°, 60°	Associated charged-particle multiplicities and correlations	74-18
Pisa- Stony Brook	γ	4.5		90°, 17°	Associated charged-particle multiplicities	74-25, 26, 27
Saclay- Strasbourg	$^{\pm}\pi, \gamma, h$	5		90°	Single-particle distributions	73-9

7.1. Single Inclusive Reactions

A compilation of pion production data at large p_t is given in Fig.

7.1. The dominant feature at large p_t is the deviation from the exponential dependence observed at smaller transverse momenta. The p_t -dependence observed at large p_t at the ISR for the production of π^0 was parametrized with a formula suggested by many models.

$$f = E \frac{d^3\sigma}{d^3p} = A p_t^{-N} e^{-B p_t / \sqrt{s}} \quad (7.1)$$

where

$$A \simeq 1.5 \times 10^{-26} \text{ cm}^2 \text{ GeV}^{N-2} \text{ sr}^{-1}$$

$$B \simeq 26.1 \pm 0.5; \quad N = 8.24 \pm 0.05$$

The energy dependence of the invariant cross sections at fixed values of p_t is schematically shown in Fig. 7.3. The curves are quite similar to those of Fig. 4.6, which involve intermediate p_t values. This may suggest a common origin for the large $-p_t$ and small $-p_t$ events as discussed at the beginning of this section: the lack of events at large- p_t and small energies would be connected with a kind of threshold effect.

From the graphs of Fig. 7.2 one can make extrapolations to $s \rightarrow \infty$ and obtain the asymptotic, or limiting p_t -distribution, which seems to have a p_t -dependence of p_t^{-6} .

The British-Scandinavian group has measured particles ratios at large p_t : they found that at large p_t heavy mass particles (kaons, nucleons and antinucleons) become very abundant comparable to pions.

7.2. Correlations Involving Large p_t -Particles

As indicated in Table 7.1 and Fig. 5.1b many experiments have been performed in which the equipment was triggered by one particle with a large p_t . Large correlation effects, larger than at smaller p_t , are observed.

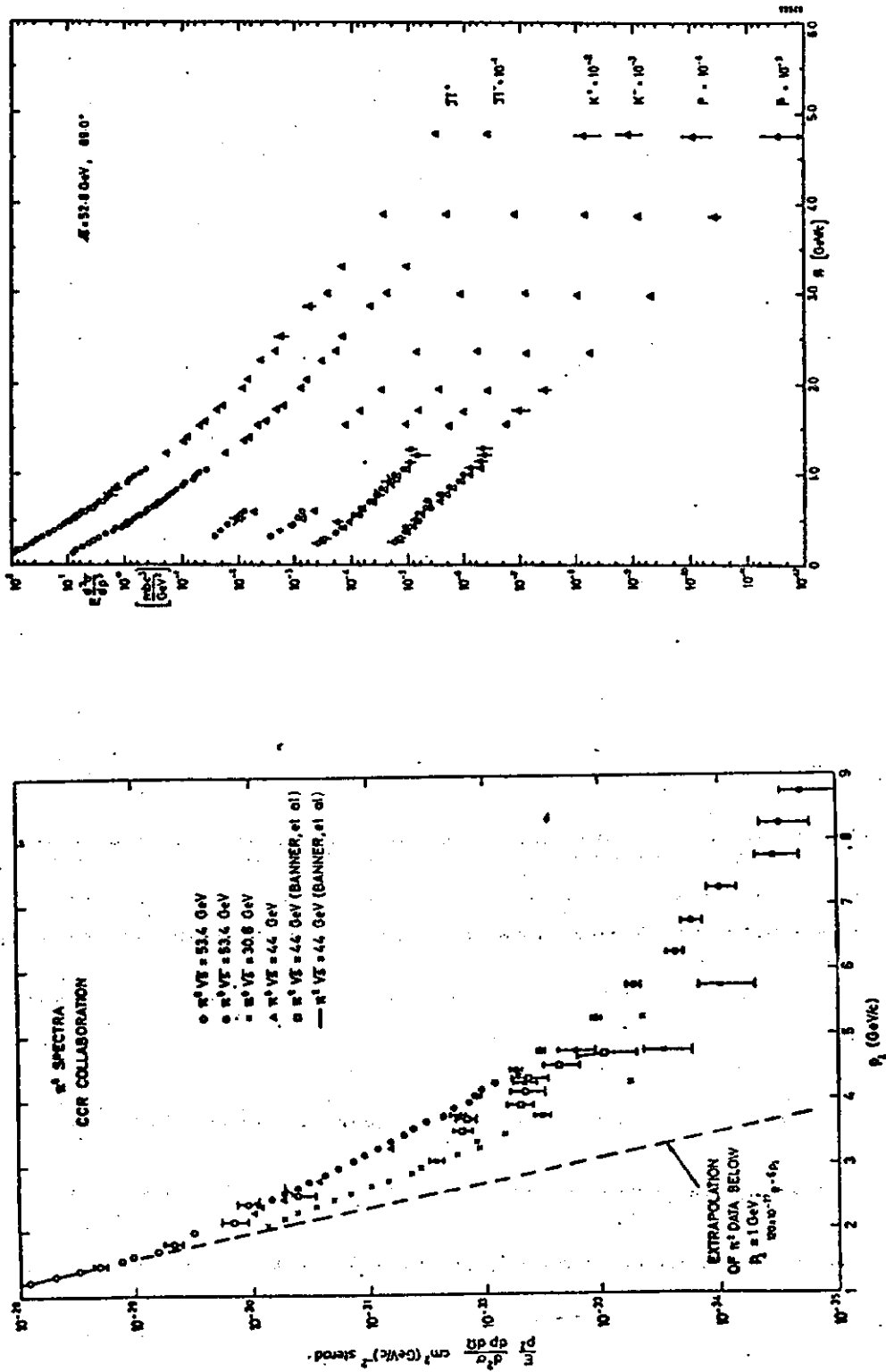


Fig. 7.1. Compilation of invariant cross-sections for pion production at large transverse momentum in pp collisions (73-7, 73-9, 73-12, 74-8).

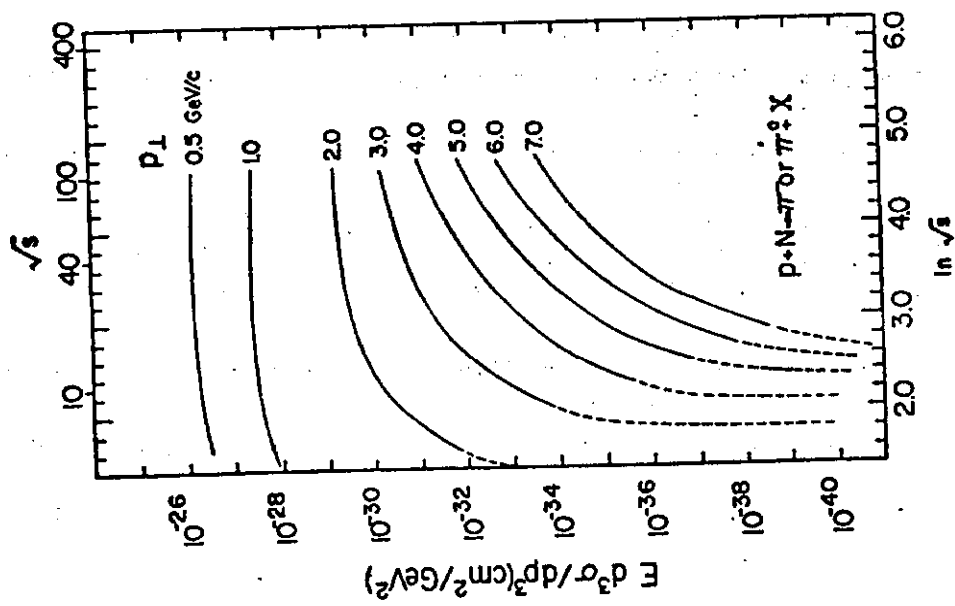


Fig. 7.2. Energy dependence of the invariant cross section for pion production of large p_t (from a compilation of J. Cronin).

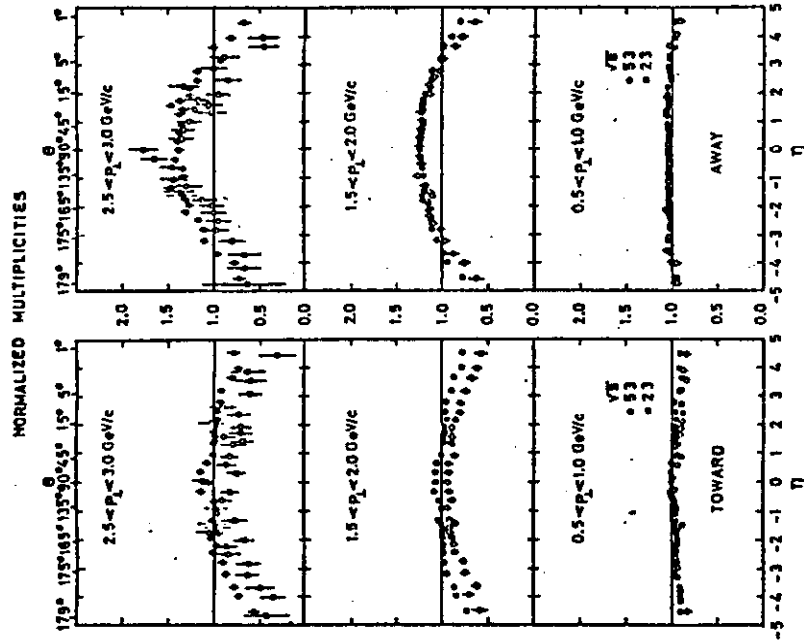


Fig. 7.3. Pseudorapidity distribution of the charge particle multiplicity associated with a large p_t^0 , normalized to the case when the p_t of the π^0 is small (74-16).

The Pisa-Stony Brook (74-16) and the ACHM (74-19) collaborations triggered their equipments, which detect charged particles, with π^0 's of large transverse momenta. Figure 7.3 shows the pseudorapidity distributions of the multiplicity of charged particles associated with the large p_t neutral pion, normalized to the multiplicities of lower p_t -events. There is a broad correlation in rapidity, which is particularly prominent when the π^0 has a larger p_t and when the charged particles are emitted on the opposite side of the π^0 . By integration of the curves, one observes that the charged multiplicity increases with the p_t of the π^0 (Fig. 7.4).

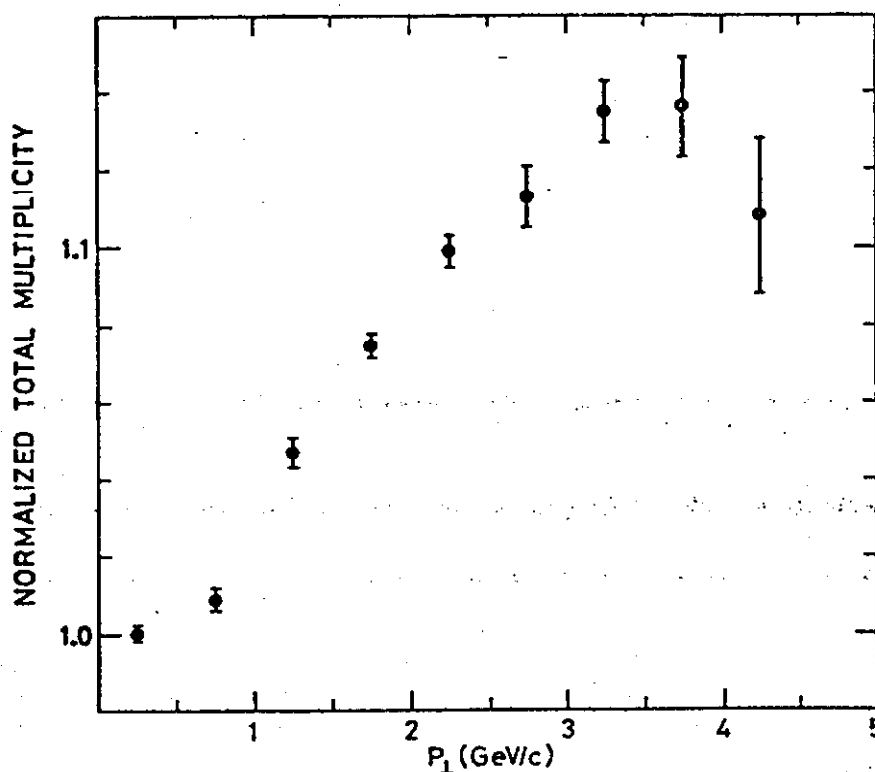


Fig. 7.4. Average total multiplicity of charged particles as a function of the transverse momentum of photons detected at 90° . The data are normalized to the multiplicity in the lowest p_t bin (74-16).

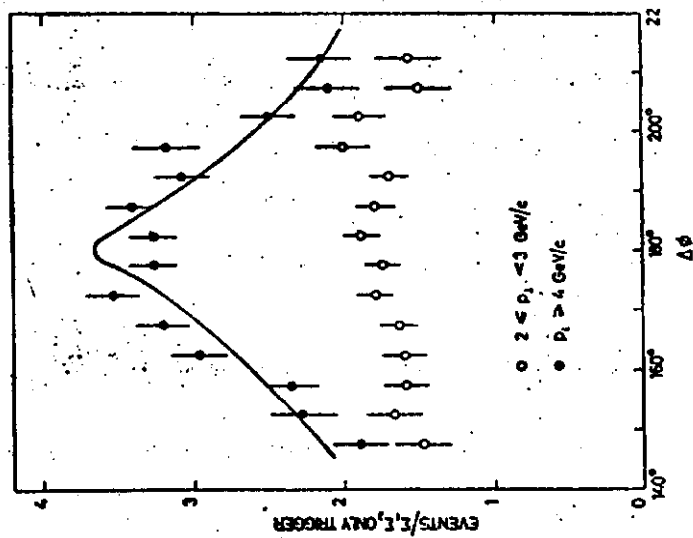


Fig. 7.5. Correlation in azimuth of charged particles emitted in the opposite hemisphere from a π^0 of large transverse momentum (74-22).

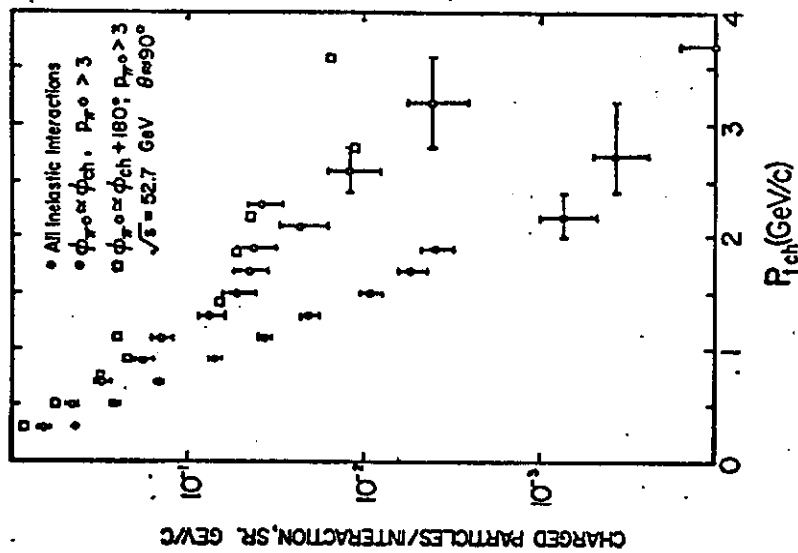


Fig. 7.6. Charged particle spectrum (a) uncorrelated (b) correlated with a π^0 with $p_t > 3$ GeV/c and $\Delta\phi = 0$ (c) with a π^0 with $p_t > 3$ GeV/c and $\Delta\phi = 180^\circ$ (74-11).

There are also correlations in azimuth, with an enhancement of $\Delta\varphi = 180^\circ$. This is particularly evident when the p_t of the π^0 is large, as shown by Fig. 7.5 (CCR collaboration, 74-22). The CCR collaboration has also done $\pi^0 - \pi^0$ correlations at 90° further confirming this result (the correlation is stronger when both π^0 's have a large p_t).

The CCRS collaboration using the magnetic spectrometers of the Saclay group and the lead glass arrays of the CCR group found a surprising result (Fig. 7.6): the correlation between a π^0 with $p_t > 3 \text{ GeV}/c$ and charged particles of various transverse momenta is strong, it increases with the p_t of the charge particles, but is independent of the azimuthal angle $\Delta\varphi$ (it is the same on the same side or opposite side of the π^0) (74-11).

8. PARTICLE SEARCHES

A number of searches for new particles have been performed or will be performed at the ISR. Compared to conventional accelerators the ISR offers the advantage of higher c.m. energies, thus allowing searches to larger masses. But the ISR has the disadvantage of having a luminosity several orders of magnitude smaller than for conventional accelerators; thus the limits in cross sections are much worse than at other accelerators.

8.1. Magnetic Monopoles

Searches for free magnetic monopoles are based on the hypothesis of large magnetic charges, according to the Dirac relation:

$$y = n \frac{137}{2} e = ng_D \quad (n = 1, 2, \dots) \quad (8.1)$$

Relativistic monopoles should ionize $4700n^2$ times the ionization of minimum ionizing particles.

Three types of monopole searches have been performed until now at the ISR. The Bologna-Rome collaboration used plastic detectors to detect the monopoles directly after this production in pp collisions. For this purpose the

I1 intersecting region was surrounded with stacks of nitrocellulose and makrofol-E sheets, covering about one-fourth of 4π and $20^\circ < \theta < 90^\circ$. Nitrocellulose sheets are sensitive to particles which ionize more than $0.8 \text{ GeV g}^{-1} \text{ cm}^2$, while the threshold for makrofol-E is $3.5 \text{ GeV g}^{-1} \text{ cm}^2$. Because of these high threshold values, plastic detectors may be used in a large background of minimum ionizing particles, the background limit being given by nuclear fragments of $Z = 2$. In the developed plates these fragments yield a general background which shows up as randomly oriented tracks at the surfaces. Consequently an area scan of the sheets, at their centers, has almost no background. The present preliminary upper limit is $3 \times 10^{-36} \text{ cm}^2$ (2 st. dev.) for monopoles with $0.5 < n < 3$ and $\text{mass} < 24 \text{ GeV}$ (74-28).

The Bologna-Fermilab collaboration has made an indirect search, trying to detect magnetic monopoles trapped in the I5 vacuum chamber and in other materials (74-29). Pieces of the vacuum chamber were placed in front of a superconducting solenoid: magnetic monopoles should have been extracted, accelerated to several GeV and detected by a number of thin scintillation counters. Other pieces of the I5 vacuum chambers were sent to Berkeley: they will be mechanically circulated in a superconducting solenoid where a monopole should appear as an induction transient.

The upper limits for monopole production will be improved in the near future, but it will be difficult to go much below 10^{-36} cm^2 .

Monopoles are also being searched for as multigamma events, by the Brookhaven-Grumman-Rome collaboration.

8.2. Quarks

Searches for free quarks are based on the hypothesis that they ionize $1/9$ or $4/9$ of minimum ionizing particles. Early searches were made by the CERN-Munich (72-8) and by the British-Scandinavian (73-11) collaborations using telescopes of scintillation counters, proportional chambers and Cerenkov counters. No quarks were found in about 10^9 observed particles. Thus the

upper limit cross sections for $m < 24$ GeV are of the order of 2×10^{-34} cm² for an isotropic quark production.

A new search for free quarks is being performed by the Bologna-CERN collaboration using the SFM facility; it should lower the cross section by one or two orders of magnitude.

8.3. Direct Lepton Production

The CCRS collaboration (R 105) has looked for the direct production of leptons of large transverse momentum, using arrays of lead glass Cerenkov counters after magnetic analysis (74-7). They found that

$$\frac{\text{direct } e^-(e^+)}{\pi^-(\pi^+)} \simeq 0.8 \times 10^{-4} \quad (8.1)$$

independent of p_t . This result is in agreement with results of similar experiments at Fermilab. The p_t -distribution of the directly produced leptons is smooth; the absolute value is larger than what one would have expected on the basis of parton models.

The British collaboration (R 204) has searched for direct muon production, placing an upper limit of 5×10^{-36} cm²/sr for μ emitted around 90° and with a $p_t > 4$ GeV/c (74-27).

8.4. Production of \bar{d}

The British-Scandinavian collaboration has found an abundant production of \bar{d} at large angles (73-11). The \bar{d}/π -ratio has increased from $\simeq 10^{-7}$ at 30 GeV, to $\simeq 10^{-6}$ at 70 GeV, $\simeq 10^{-5}$ at 300 GeV and 5×10^{-4} at ISR energies. Moreover while at lower energies the \bar{d} were produced in p-Nuclei collisions, at the ISR they are produced in pp collisions. The p_t -dependence of the invariant cross section for \bar{d} production at the ISR seems to be less steep

than for \bar{p} : thus the slope seems to decrease with increasing mass. These features give problems to various mechanisms of production of antinuclei. In fact it would seem that the \bar{d} is produced via a statistical mechanism which does not differ from that of other particles.

9. CONCLUSIONS

The experimental results from the CERN-ISR have given an almost complete picture of pp interactions at high energies. Let us summarize the main features and some interpretations:

1. The pp total cross section rises approximately as $\ln^2 s$ (by about 10% in the ISR range).
2. The ratio ρ of real to imaginary part of the forward scattering amplitude becomes positive above 200 GeV/c.
3. Elastic scattering is consistent with a geometrical picture of the nucleon, with a kind of an inner region and a skin. The shrinking of the diffraction pattern continues to the highest energies.
4. Most of the pp interactions lead to inelastic processes, which may be broadly classified in diffractive and central processes. The ensemble of inelastic events are characterized by a small and almost energy independent value of $\langle p_t \rangle$ and by logarithmically rising multiplicities.
5. Diffractive processes result in a small number of produced particles, while central processes result, on the average, on the production of a larger number of particles.
6. The study of large p_t -events has not yet allowed to establish if they are interpretable in terms of constituent models or of more conventional models not involving nuclear substructures.
7. There are all sort of correlations, in rapidity, in ϕ , in p_t , etc. between the final state products. This suggests that the production process is a complicated one and occurs probably as a two step process:

first a number of clusters (or fireballs or N^* or other states) are produced; then these states decay into the observed particles. If clusters occur they probably have masses of 2-2.5 GeV and decay into 2-4 particles.

8. Some exclusive processes of the diffractive type have been observed. Their t -distributions exhibit shrinking, which thus seems to be a general phenomenon, not only associated with elastic scattering.
9. No new particle has been observed.
10. There is no model which explains all the observed features; instead each model explains a small amount of data.

The above features indicate that we are still far away from the asymptotic region, where "all asymptotic theorems come true." In particular the presently established trend of $\rho = \text{Re}/\text{Im}$ indicates that ρ has become positive; it is expected that, as the energy increases, ρ will reach a maximum and then will decrease towards zero from positive values. It would seem that the asymptotic region cannot start before the start of the falling down of ρ , that is that the asymptotic region may start only at laboratory momenta of several thousand GeV.

Present and future experiments at the ISR should confirm with more precision the above statements and the interpretations which follow. But it may be expected, in general, that the new experiments will look more and more for specific details and will have to be guided by specific models. The experimental study of the properties of the asymptotic region may very well have to wait for an even higher energy accelerator.

10. Acknowledgments

I would like to thank very many colleagues for making available their data and for explaining them. A number of discussions is gratefully acknowledged. I benefitted very much from the ISR discussion meetings between experimentalists and theorists organized by M. Jacob and from the lecture notes of M. Albrow, J. Allaby, U. Amaldi, G. Cocconi, J. Cronin, A. Diddens, G.V. Dardel, J. Sens and A.M. Wetherell.

References

The following is a complete list of the experimental papers published by ISR teams. For other references on the subject the reader is referred to the Proceedings of the 1974 London Conference and to the individual papers listed below.

- 71-1 PL 34B (1971) p. 425. First observation of colliding beam events at the CERN Intersecting Storage Rings (ISR). The ISR Staff.
- 71-2 PL 35B (1971) p. 355. Observations of small angle proton-proton elastic scattering at 30 GeV and 45 GeV centre-of-mass energies.
R602 Aachen-CERN-Genova-Harvard-Torino, M. Holder et al.
- 71-3 PL 35B (1971) p. 361. Determination of the proton-proton elastic cross section at 30 GeV centre-of-mass energy.
602 Aachen-CERN-Genova-Harvard-Torino, M. Holder et al.
- 71-4 PL 36B (1971) p. 400. Further results on small angle elastic proton-proton scattering at very high energies.
R602 Aachen-CERN-Genova-Harvard-Torino, M. Holder et al.
- 71-5 PL 36B (1971) p. 504. Measurements of small angle proton-proton elastic scattering at the CERN Intersecting Storage Rings.
R601 CERN-Rome, U. Amaldi et al.
- 71-6 PL 36B (1971) p. 611. Angular distribution of secondary particles produced in the Intersecting Storage Rings at an energy equivalent to 1500 GeV.
R101 Bombay-CERN-Cracow (no names).
- 71-7 PL 37B (1971) p. 438. Transverse momentum distribution of photons produced in proton-proton collisions at the Intersecting Storage Rings.
R404T CERN-Hamburg-Vienna, G. Neuhofer et al.
- 71-8 PRL 27 (1971) p. 68. Proton-proton inelastic scattering at very high energies.
R202 Argonne-Bologna-Michigan, L.G. Ratner et al.

- 72-1 PL 38B (1972) p. 51. Single γ -ray spectra from proton-proton collisions at centre-of-mass energies from 30 to 50 GeV.
R404T CERN-Hamburg-Vienna, G. Neuhofer et al.
- 72-2 PL 38B (1972) p. 260. Negative particle production at the CERN Intersecting Storage Rings.
R202 Bologna, A. Bertin et al.
- 72-3 PL 39B (1972) p. 294. Experimental observation of the angular distribution of charged particles around 90° in the centre-of-mass produced by proton-proton collisions at very high energies.
R602 Aachen-CERN-Genova-Harvard-Torino, G. Barbiellini et al.
- 72-4 PL 39B (1972) p. 654. Angular distribution of charged particles between 30° and 90° produced in pp collisions at ISR energies.
R403 CERN-Hamburg-Orsay-Vienna, M. Breidenbach et al.
- 72-5 PL 39B (1972) p. 663. Small angle proton-proton elastic scattering at very high energies ($460 \text{ GeV}^2 < s < 2900 \text{ GeV}^2$).
R602 Aachen-CERN-Genova-Harvard-Torino, G. Barbiellini et al.
- 72-6 PL 40B (1972) p. 136. Particle production ratios at 21, 31, 45 and 53 GeV in the centre of mass.
R201 CERN-Holland-Lancaster-Manchester. M.G. Albrow et al.
- 72-7 PL 40B (1972) p. 507. The angular distribution of charged particles produced in pp collisions at the CERN Intersecting Storage Rings.
R101 Cracow-CERN, J. Babecki et al.
- 72-8 PL 40B (1972) p. 693. A search for quarks at the CERN Intersecting Storage Rings.
R402 CERN-Munich, M. Bott-Bodenhausen et al.
- 72-9 PL 41B (1972) p. 201. Charged particle production ratios at the CERN ISR for a transverse momentum of $0.4 \text{ GeV}/c$.
R202 Bologna-CERN, A. Bertin et al.
- 72-10 PL 41B (1972) p. 221. Wide angle production of slow antiprotons at the CERN Intersecting Storage Rings.
R101 Bucharest-CERN, B. Bogdan et al.

- 72-11 PL 41B (1972) p. 547. Charged particle production at 90° in the centre of mass in very high energy proton-proton collisions.
R102 Saclay-Strasbourg, M. Banner et al.
- 72-12 PL 42B (1972) p. 279. The distribution in transverse momentum of 5 GeV/c secondaries produced at 53 GeV in the centre of mass.
R201 CERN-Holland-Lancaster-Manchester, M.G. Albrow et al.
- 72-13 PL 42B (1972) p. 493. Charged particle production at the CERN ISR as a function of transverse momentum.
R202 Bologna-CERN, A. Bertin et al.
- 73-1 PL 43B (1973) p. 231. Measurements of proton-proton total cross section by means of Coulomb scattering at the CERN Intersecting Storage Rings.
R601 CERN-Rome, U. Amaldi et al.
- 73-2 PL 44B (1973) p. 112. The energy dependence of the proton-proton total cross section for centre-of-mass energies between 23 and 53 GeV.
R601 CERN-Rome, U. Amaldi et al.
- 73-3 PL 44B (1973) p. 119. Measurements of the total proton-proton cross section at the ISR.
R801 Pisa-Stony Brook, S.R. Amendolia et al.
- 73-4 PL 44B (1973) p. 207. Correlations associated with small angle protons produced in proton-proton collisions at 31 GeV total energy.
R201 CERN-Holland-Lancaster-Manchester, M.G. Albrow et al.
- 73-5 PL 44B (1973) p. 313. Rapidity correlations in inclusive two-particle production at storage ring energies.
R404T CERN-Hamburg-Vienna, H. Dibon et al.
- 73-6 PL 44B (1973) p. 518. Correlation between the pionization region and the fragmentation region in high energy proton-proton collisions.
R201 CERN-Holland-Lancaster-Manchester, M.G. Albrow et al.

- 73-7 PL 44B (1973) p. 521. Production of high transverse momentum particles in p-p collisions in the central region at the CERN ISR.
R203 British-Scandinavian, B. Alper et al.
- 73-8 PL 44B (1973) p. 527. Particle composition at high transverse momenta in pp collisions in the central region at the CERN ISR.
R203 British-Scandinavian, B. Alper et al.
- 73-9 PL 44B (1973) p. 537. Large transverse momentum particle production at 90° in proton-proton collisions at the ISR.
R102. Saclay-Strasbourg, M. Banner et al.
- 73-10 PL 45B (1973) p. 69. Experimental tests of limiting fragmentation at the ISR.
R801 Pisa-Stony Brook, G. Bellettini et al.
- 73-11 PL 46B (1973) p. 265. Large angle production of stable particles heavier than the proton and a search for quarks at the CERN Intersecting Storage Rings.
R203. British-Scandinavian, B. Alper et al.
- 73-12 PL 46B (1973) p. 471. Observation of π^0 mesons with large transverse momentum in high energy proton-proton collisions.
R103 CERN-Columbia-Rockefeller, F.W. Büsler et al.
- 73-13 PL 47B (1973) p. 75. Large-angle inclusive production of charged pions at the CERN ISR with transverse momentum less than 1.0 GeV/c.
R203 British-Scandinavian, B. Alper et al.
- 73-14 PL 47B (1973) p. 275. Large-angle inclusive production of protons, antiprotons and kaons, and particle composition of the CERN ISR.
R203 British-Scandinavian, B. Alper et al.
- 73-15 NP B51 (1973) p. 388. Longitudinal momentum distributions for positive particles produced at small angles in proton-proton collisions at a c.m. energy of 44.6 GeV.
R201 CERN-Holland-Lancaster-Manchester, M.G. Albrow et al.

- 73-16 NP B54 (1973) p. 6. The spectrum of protons produced in pp collisions at 31 GeV total energy.
R201 CERN-Holland-Lancaster-Manchester, M.G. Albrow et al.
- 73-17 NP B56 (1973) p. 333. Negative particle production in the fragmentation region at the CERN ISR.
R201 CERN-Holland-Lancaster-Manchester, M.G. Albrow et al.
- 73-18 NP B63 (1973) p. 45. Study of $pp \rightarrow \gamma + \text{anything}$ at the ISR at $E_{\text{cm}} = 44.4$ GeV and its implications for π^0 production and multiplicity.
R101 Tata Institute, R.R. Daniel, et al.
- 73-19 Nuovo Cim. 17A (1973) p. 735. Total cross section measurement at the ISR.
R801 Pisa-Stony Brook, S.R. Amendolia et al.
- 73-20 Lettere al Nuovo Cim. 6 (1973) 121. Multiplicities of charged particles up to ISR energies.
R202 Bologna-CERN, M. Antinucci et al.
- 74-1 PL 48B (1974) p. 359. Measurement of inclusive two-particle rapidity correlations at the ISR.
R801 Pisa-Stony Brook, S.R. Amendolia et al.
- 74-2 PL 48B (1974) p. 371. A search for large transverse momentum electrons at the CERN-ISR.
R103 CERN-Columbia-Rockefeller, F.W. Büsler et al.
- 74-3 PL 49B (1974) p. 491. Observation of a diffraction minimum in the proton-proton elastic scattering at the ISR.
R602 Aachen-CERN-Harvard-Genova-Torino, A.M. Böhm et al.
- 74-4 NP B70 (1974) p. 1. Transverse momentum dependence in pp inclusive reactions at very high energies.
R202 Bologna-CERN, P. Capiluppi et al.
- 74-5 NP B73 (1974) p. 40. Positive particle production in the fragmentation region at the CERN-ISR.
R201 CERN-Holland-Lancaster-Manchester, M.G. Albrow et al.

74-6 PR D9 (1974) p, 1135. Measurement of pp inclusive cross sections at very high energy.

R202 Argonne-Bologna-Michigan, L.G. Ratner et al.

The following papers were presented at the 17th International Conference on High Energy Physics, London, 1-10 July 1974.

74-7 Paper 218: Search for electrons of large transverse momentum at the CERN-ISR.

R103 CERN-Columbia-Rockefeller-Saclay Coll.

74-8 Paper 227: Single inclusive charged particle production at high p_t at the CERN-ISR.

R203 British-Scandinavian Coll., B. Alper et al.

74-9 Paper 228: Correlations between charged particles and one momentum analyzed forward negative particle at the ISR.

R801, R802 CERN-Pisa-Rome-SUNY Coll., J.V. Allaby et al.

74-10 Papers 463, 987: Wide angle transverse momentum correlations at the CERN-ISR.

R102 Saclay, M. Banner et al.

74-11 Paper 464: Inclusive spectra and correlations at large p_t .

R105 CCRS Coll.

74-12 Paper 487: Search for heavy mass particles of integral charge in the fragmentation region at the CERN-ISR.

R201, CHLM Coll., M.G. Albrow et al.

74-13 Paper 488: Experimental results on large-angle elastic pp scattering at the CERN-ISR.

R401 CERN-Hamburg-Orsay-Vienna (CHOV) Coll., E. Nagy, et al.

74-14 Paper 489: Experimental results on inelastic diffraction scattering in pp collisions at the ISR.

R401 CHOV Coll., E. Nagy, et al.

- 74-15 Paper 514: Clustering of charged secondaries in pp collisions at the ISR.
R801 Pisa-SUNY Coll., S.R. Amendolia, et al.
- 74-16 Papers 515, 988, 990: Measurements of charged particle multiplicities emitted in association with a large p_t photon in pp interactions at the ISR.
R801 Pisa-SUNY Coll., G. Bellettini et al.
- 74-17 Paper 548: Inclusive two charged particle correlations in pp collisions at the CERN ISR at total energies of 45 and 53 GeV.
R206 CHLM Coll., M.G. Albrow et al.
- 74-18 Paper 549: Charged multiplicity associated with particles of high transverse momentum in the central region.
R205 CERN-British Universities Coll., B. Alper et al.
- 74-19 Paper 590: Observation of proton-proton interactions with π^0 's of large transverse momentum at the ISR.
R701 Aachen-CERN-Heidelberg-Munich Coll., H. Albrecht et al.
- 74-20 Paper 591: Observation of inelastic proton-proton collisions at the ISR with a streamer chamber.
R701 Aachen-CERN-Heidelberg-Munich Coll., H. Albrecht et al.
- 74-21 Paper 592: Production of π^0 's with large transverse momentum at the ISR.
R701 ACHM Coll., B. Betev et al.
- 74-22 Paper 728: Correlations between large transverse momentum π^0 mesons and charged particles or π^0 mesons at the CERN ISR.
R103 CCR Coll., F.W. Busser et al.
- 74-23 Paper 929: Charged particle production in proton-proton inclusive reactions at very high energies.
R202 Bologna-CERN-Coll., P. Capiluppi et al.
- 74-24 Paper 987: Transverse momentum correlations of secondaries produced at large angles at the ISR.
R102 Saclay, M. Banner et al.

- 74-25 Paper 1021: Correlations in quasi-elastic pp scattering at total c.m. energies of 23 and 31 GeV.
R206 CDHLM Coll., M. G. Albrow et al.
- 74-26 Paper 1014: Measurements of $pp \rightarrow (p\pi^+\pi^-) + X$ at the CERN ISR; Scaling tests and evidence for double excitation.
R603 Aachen-CERN-UCLA Coll., L. Backsay et al.
- 74-27 Paper 1050: Search for muons with high transverse momentum at the CERN Intersecting Storage Rings.
R204 British Universities Coll., R. Birge et al.
- 74-28 Search for magnetic monopoles at the CERN ISR with the plastic detector technique.
R106 Bologna-Rome Coll., G. Baroni et al.
- 74-29 Search for magnetic monopoles at the CERN ISR.
R106 Bologna-Fermilab Coll., R.A. Carrigan et al.
- 73-40 Experimental study of the energy dependence in pp inclusive reactions.
R202 Bologna-CERN-Padova Coll., A.M. Rossi et al.
- 74-31 Proton diffraction dissociation studies at the CERN ISR.
R602 ACGHT Coll., A. Bohm et al.
- 74-32 Aachen-CERN-Harvard-UCR Coll.

Notations:

PL = Physics Letters
PRL = Physical Review Letter
NC = Nuclear Physics B
PR = Physical Review